Journal of Controlled Release 391 (2026) 114607

Contents lists available at ScienceDirect

Journal of Controlled Release

journal homepage: www.elsevier.com/locate/jconrel

Optimized lipid nanoparticles for pulmonary delivery of CRISPR/Cas9 targeting KRAS G12S in lung cancer☆

Moritz Marschhofer [a], Siyu Chen [a], Müge Molbay [a,g], Benjamin Winkeljann [a,f,g,h,i], Ersilia Villano [a,j], Corinne Giancaspro [a], Alexandra Kourou [a], Otto Berninghausen [b], Susanne Rieder [b], Charlotte Ungewickell [b], Roland Beckmann [b], Bastian Popper [c], Ana Maria Torres [d], Anxo Vidal [e], Olivia M. Merkel [a,f,g,i], Simone P. Carneiro [a,g,h,*]

[a] Ludwig-Maximilians-Universität München, Department of Pharmacy, Pharmaceutical Technology and Biopharmaceutics, Munich 81377, Germany
[b] Gene Center and Department of Biochemistry, Ludwig-Maximilians-Universität München, Munich 81377, Germany
[c] Biomedical Center, Core Facility Animal Models, Medical Faculty, Ludwig-Maximilians-Universität München, Martinsried 82152, Germany
[d] Experimental Biomedicine Centre (CEBEGA), University of Santiago de Compostela, Santiago de Compostela 15706, Spain
[e] Center for Research in Molecular Medicine and Chronic Diseases (CiMUS), Health Research Institute of Santiago de Compostela (IDIS), University of Santiago de Compostela, Santiago de Compostela 15782, Spain
[f] Department of Pharmacy, Ludwig-Maximilians-Universität München, Member of the German Center for Lung Research (DZL), Munich, Germany
[g] Center for NanoScience (CeNS), Ludwig-Maximilians-Universität München, Munich 80799, Germany
[h] Pharmaceutical Engineering and Technology Research Scientists (PETRS), Germany
[i] RNhale GmbH, Am Klopferspitz 19, Planegg 82152, Germany
[j] University of Naples Federico II, Department of Pharmacy, Naples 80131, Italy

ARTICLE INFO

Keywords:
Lipid nanoparticles
Pulmonary administration
Non-small cell lung cancer
CRISPR/Cas9 delivery
KRAS mutation

ABSTRACT

KRAS G12S mutations in non-small cell lung cancer (NSCLC) remain refractory to current targeted therapies, with few clinical options and frequent resistance. While CRISPR/Cas9 enables mutation-specific gene disruption, its pulmonary application is limited by systemic clearance, hepatic tropism, and airway mucus barriers. Here, we present lipid nanoparticles (LNPs) specifically engineered for pulmonary delivery of Cas9 mRNA and KRAS G12S-targeting sgRNA, optimized through mRNA surrogate screening and orthogonal mixture design to guide lipid composition and Cas9:sgRNA weight-to-weight ratios. Two lead LNP formulations, A6 3:1 and A8 1:1, exhibited robust critical quality attributes, including particle sizes below 120 nm, low polydispersity, near-neutral zeta potential, and over 80 % encapsulation efficiency. Cryo-TEM revealed distinct morphologies correlated with enhanced transfection. *In vitro*, A8 1:1 achieved up to 90 % on-target gene editing in A549 cells and a 3.6-fold increase in apoptosis, while A6 3:1 induced a 3.7-fold apoptotic response. Both formulations efficiently traversed airway mucus in air-liquid interface cultures and preserved over 80 % cell viability across doses. *In vivo*, repeated pulmonary administration was well tolerated, with no signs of systemic toxicity or cytokine elevation in healthy or tumor-bearing mice. In an orthotopic A549-luc lung tumor model, intratracheal delivery of A6 3:1 and A8 1:1 modestly suppressed tumor growth, with histological evidence of tumor cell apoptosis for A8 1:1. Quantification confirmed a statistically significant increase of apoptosis in the A8 1:1 group, consistent with effective *KRAS* disruption *in vivo*. Overall, lead LNPs, particularly A8 1:1, enabled efficient and localized RNA-based gene editing that induced downstream apoptotic signaling, demonstrating a preliminary, yet promising, proof-of-concept for CRISPR/Cas9 therapy in NSCLC.

☆ This article is part of a Special issue entitled: 'Young Investigator Issue' published in Journal of Controlled Release.

* Corresponding author at: Ludwig-Maximilians-Universität München, Department of Pharmacy, Pharmaceutical Technology and Biopharmaceutics, Munich 81377, Germany.
E-mail address: simone.carneiro@cup.uni-muenchen.de (S.P. Carneiro).

https://doi.org/10.1016/j.jconrel.2026.114607
Received 21 August 2025; Received in revised form 12 December 2025; Accepted 5 January 2026
Available online 6 January 2026

1. Introduction

Lung cancer ranks among the most prevalent malignancies, accounting for nearly 1.8 million deaths worldwide in 2020, which corresponds to approximately 20 % of all cancer-related mortality [1]. Oncogenic driver mutations in genes such as epidermal growth factor receptor (*EGFR*), anaplastic lymphoma kinase (*ALK*), and *ERBB2* [2] are well-documented. Yet, mutations in the *KRAS* oncogene are the most frequent and present in about 25 % of all non-small cell lung cancer (NSCLC) cases, with the G12C point mutation being the most common [3]. While therapies for *EGFR* or *ALK* mutations have significantly improved patient outcomes, targeted therapies for *KRAS* mutations have historically been limited [4,5]. The approval of two KRAS G12C-specific inhibitors for the treatment of NSCLC, namely Sotorasib and Adagrasib, by the U.S. Food and Drug Administration (FDA) represents a major therapeutic advance. These covalent inhibitors selectively bind to the cysteine residue at position 12 within the switch II pocket of the GDP-bound KRAS protein, locking it in an inactive state and preventing downstream oncogenic signaling [6,7]. Despite their clinical efficacy, these therapies are limited to patients harboring the G12C mutation and are typically administered after prior systemic therapy, leaving the majority of *KRAS*-mutated cases without selective treatment [3,6,7]. Moreover, the reliance on a unique amino acid for inhibition is associated with susceptibility to acquired resistance, observed in nearly half of treated patients [8]. Common resistances include secondary *KRAS* mutations (*e.g.*, G12D, G13D, G12S), alterations in the drug binding-pocket (*e.g.*, Y96C), bypass signaling *via* MET, NRAS, BRAF, or RET, and histologic transformation [8–10]. Given these challenges, there is a clear need for broader and more durable therapeutic strategies capable of overcoming resistance and targeting a wider spectrum of *KRAS* mutations.

Clustered regularly interspaced short palindromic repeats (CRISPR)/Cas9, originally part of the bacterial immune system against phages, has become a powerful and versatile genome-editing tool. When paired with a single guide RNA (sgRNA), the complex can selectively bind to target DNA sequences and induce site-specific double-strand breaks [11,12]. These breaks are primarily repaired by non-homologous end joining (NHEJ), a process that directly ligates the DNA ends but is prone to errors. As a result, insertions or deletions (indels) frequently occur [13], often disrupting the coding sequence and leading to loss of protein function [14]. This mechanism can be used to selectively disrupt mutated *KRAS* and suppress further tumor growth. Moreover, the system allows for rapid adaptation. The emergence of novel or uncommon mutations can be readily addressed by redesigning the sgRNA.

Despite the therapeutic promise of CRISPR/Cas9 for the treatment of NSCLC, efficient delivery remains challenging. CRISPR/Cas9 delivery can be achieved through several strategies: (i) direct delivery of the Cas9/sgRNA ribonucleoprotein complex, in which the Cas9 protein is pre-assembled with the sgRNA prior to administration, (ii) plasmid DNA encoding both Cas9 and the sgRNA, or (iii) mRNA encoding Cas9 in combination with a separate sgRNA [15]. Direct cellular uptake of proteins is inherently inefficient, and their purification is both technically demanding and cost-intensive [15,16]. An attractive alternative is the use of mRNA encoding Cas9, which enables transient protein expression and, thereby, minimizes the risk of off-target genome editing. Unlike plasmid DNA, mRNA does not integrate into the host genome and can undergo multiple rounds of translation, enhancing indel formation while requiring less input material. Additionally, mRNA is generally less immunogenic than plasmid DNA or the Cas9 protein, making it more suitable for therapeutic applications [17].

Lipid nanoparticles (LNPs) have transformed nucleic acid delivery by protecting mRNA from degradation and enabling efficient cell uptake and cytoplasmic release [18–20]. This technology has been successfully applied to deliver CRISPR/Cas9 components, demonstrating therapeutic efficacy in preclinical models, including the suppression of VEGFR2-expressing lung tumors in mice [21]. The recent FDA approval of Casgevy®, the first CRISPR/Cas9-based therapy for sickle cell disease and beta-thalassemia, further validates the clinical potential of genome editing technologies [22]. Extending these breakthroughs, LNP-mediated delivery of CRISPR/Cas9 is now being explored through clinical trials across a broad spectrum of indications, including metabolic, immunological, and cardiovascular diseases [23–25].

The success of mRNA vaccines against COVID-19 has demonstrated the safety, scalability, and clinical impact of LNP platforms, establishing them as suitable vehicles for RNA therapeutics, including Cas9 mRNA and sgRNA [18,19]. Both research-grade and FDA-approved formulations rely on lipid compositions originally introduced in Onpattro® [26], the first siRNA-based drug approved for hereditary transthyretin-mediated amyloidosis. Onpattro's formulation was optimized for hepatic delivery [27], taking advantage of the natural tropism of LNPs for hepatocytes *via* apolipoprotein *E*-mediated uptake. While highly effective for liver-targeted therapies, this intrinsic hepatic tropism presents a major barrier for pulmonary applications such as lung cancer.

This limitation is particularly critical in lung-targeted therapies, where systemic administration fails to engage the epithelial compartment. Instead of reaching the airway epithelium, intravenously delivered LNPs accumulate in the pulmonary vasculature, leading to capillary entrapment and thrombus formation, as previously demonstrated [28]. These findings reveal a key limitation of conventional delivery routes and emphasize the need to circumvent vascular barriers. Pulmonary administration *via* intratracheal or aerosolized delivery offers a transformative alternative by enabling direct epithelial deposition, minimizing off-target accumulation, and maximizing the therapeutic efficacy of RNA-based interventions for respiratory diseases [29]. Moreover, the lung's vast surface area, thin epithelial barrier, and rich vascularization create a uniquely permissive environment for rapid uptake and localized action, making it an ideal gateway for gene editing, immunomodulation, and regenerative therapies [30].

To address the unmet clinical need in *KRAS* G12S-driven lung cancer, this study aims to employ a rational optimization strategy to refine LNP formulations for efficient pulmonary delivery of CRISPR/Cas9. Downstream functional effects, including apoptosis, were evaluated as indicators of targeted gene disruption in the lung. We first screened lipid molar ratios to identify compositions that maximize mRNA delivery efficiency. These were further refined by optimizing the weight-to-weight (*w*/w) ratios of Cas9 mRNA and sgRNA to enhance gene editing performance. Each formulation underwent thorough physicochemical characterization, including particle size, polydispersity index (PDI), zeta potential, and encapsulation efficiency, and was evaluated *in vitro* for *KRAS* G12S gene editing, downstream signaling disruption, and transport performance under mucin-producing conditions mucus. Finally, the most promising candidates were assessed *in vivo via* pulmonary administration, where they demonstrated favorable tolerability and effective apoptosis induction. This proof-of-concept study establishes its potential as a non-invasive therapeutic strategy for KRAS-driven lung cancer.

2. Materials and methods

2.1. Materials

The ionizable lipid 1-octylnonyl 8-[(2-hydroxyethyl)[6-oxo-6-(undecyloxy)hexyl]amino]octanoate (SM-102) was purchased from MedChemExpress (New Jersey, USA), while cholesterol, (1,2-distearoyl-sn glycero-3-phosphocholine (DSPC)), and (1,2 dimyristoyl-rac-glycero-3-methoxypolyethylene glycol-2000 (DMG-PEG2000)) were obtained from Sigma-Aldrich (Taufkirchen, Germany). CleanCap® Cas9 mRNA (5 moU) was bought from TriLink Biotechnologies (California, USA). Enhanced green fluorescent protein (eGFP) mRNA and Alexa Fluor 647-labeled eGFP mRNA were acquired from Ribopro (Maastricht, Netherlands). Vivaspin 6 columns (10 kDa MWCO) were purchased from Cytiva (Marlborough, USA). DNeasy blood & tissue kit was bought from

QIAGEN (Venlo, Netherlands). Propidium Iodide solution and the LEGENDplex™ MU Th Cytokine Panel were purchased from BioLegend (San Diego, USA). The TUNEL Assay Kit - HRP-DAB was acquired from Abcam (Cambridge, United Kingdom). Droplet generation oil, ddPCR supermix for probes, ddPCR primers G12S NEHJ, DG8™ cartridges, and gaskets were obtained from Bio-Rad (California, USA). PCR primers (F: TTTGAGAGCCTTTAGCCGC, R: TCTACCCTCTCACGAAACTC) and primers for Sanger sequencing (F: TCTTAAGCGTCGATGGAG, R: ACAGAGAGTGAACATCATGG) were purchased from Sigma-Aldrich (Taufkirchen, Germany). Dulbecco's Phosphate Buffered Saline (PBS), Fetal Bovine Serum (FBS), KRAS G12S sgRNA (5′- CUUGUGGUAGUUGGAGCUAG-3′), Pur-A-Lyzer™ Maxi 3500 molecular weight cut-off (MWCO), RPMI-1640, sodium acetate, 100× Tris-EDTA buffer solution, cell counting kit 8 (CCK-8), Dulbecco's Modified Eagle Medium (DMEM) high glucose medium, Eagle's MEM, MEM non-essential amino acid solution (NEAA), and Triton™ X-100 were purchased from Sigma-Aldrich (Taufkirchen, Germany). PBS 10×, absolute ethanol molecular biology grade, Gibco™ Opti-MEM™ reduced serum, Gibco™ Penicillin-Streptomycin (P/S), Quant-it™ RiboGreen RNA reagent, Annexin V-AF488, Phusion Green Hot Start II High-Fidelity PCR Mastermix, ExoSAP-IT Express PCR Product Cleanup Reagent, Lipofectamine 2000, GeneRuler 1 kb Plus DNA Ladder, and trypsin-EDTA (0.05 %) phenol red were purchased from Thermo Fisher Scientific (Darmstadt, Germany).

2.2. Methods

2.2.1. LNP preparation

eGFP mRNA-LNPs and CRISPR/Cas9-LNPs were prepared by ethanol dilution with varied molar ratios of ionizable, helper, and cholesterol lipids (Table 1). Briefly, SM-102, DSPC, Cholesterol, and DMG-PEG2000 were dissolved in absolute ethanol, combined as specified in Table 1, and diluted to a total lipid concentration of 1 mM for preparation using syringe pumps (NE-1600, New Era Pump Systems, NY, USA) connected to a microfluidic T-junction mixing (Idex P-888, Illinois, USA) or 5 mM for preparation using impingement jet mixing with the Knauer Nano-Scaler® (Berlin, Germany). For eGFP mRNA-LNPs, a 25 mM sodium acetate buffer (pH 4.0) was used to dilute the eGFP mRNA to achieve a final N/P of 6. CRISPR/Cas9-LNPs were prepared by mixing Cas9 mRNA with *KRAS* G12S sgRNA (hereafter referred to as sgRNA for simplicity). Unless otherwise stated, *KRAS* G12S was used; any deviations, such as the use of a negative control sgRNA, are explicitly indicated. All formulations employed defined *w*/w ratios, using the same buffer and the same final N/P ratio of 6.

LNPs for *in vitro* experiments were formulated using syringe pumps at a total flow rate of 3 ml/min and an aqueous-to-organic phase flow rate ratio of 3:1. For animal experiments, CRISPR/Cas9-LNPs were prepared using the Knauer Nanoscaler® at a total flow rate of 10 ml/min, maintaining the same aqueous-to-organic phase flow rate ratio. Subsequently, the formulations were dialyzed overnight at 4 °C against 1× PBS using a Pur-A-Lyzer™ Maxi Dialysis kit 3.5 kDa MWCO. Following formulation, the LNPs intended for *in vivo* studies were further concentrated using Vivaspin 6 spin columns (MWCO 10,000 Da) at 4000 rpm for 60 min to achieve the desired dosing concentration. The LNPs were sterile-filtered through 0.22 µm polyethersulfone (PES) membranes (Pall Corporation, New York, USA), and stored at 4 °C for up to 30 days.

Table 1
Molar lipid composition (%) of LNP formulations.

Formulation	SM-102 [%]	Cholesterol [%]	DSPC [%]	DMG-PEG2000 [%]
A1	20.00	19.00	59.50	1.5
A2	50.00	38.50	10.00	1.5
A3	50.00	19.00	29.50	1.5
A4	35.00	38.50	25.00	1.5
A5	20.00	38.50	40.00	1.5
A6	20.00	29.50	49.00	1.5
A7	50.00	27.90	20.60	1.5
A8	35.90	19.00	43.60	1.5
A9	35.00	28.75	34.75	1.5
B12	26.75	29.20	42.55	1.5
B13	28.60	19.00	50.90	1.5
B14	20.00	24.25	54.25	1.5
B16	27.75	24.00	46.75	1.5
B17	35.70	23.20	39.60	1.5

2.2.2. Formulation optimization

To identify the most effective LNP formulations for CRISPR/Cas9 delivery, we first conducted a preliminary screening using eGFP mRNA-LNPs. This surrogate system enabled rapid evaluation of transfection efficiency and physicochemical properties across varying lipid compositions. An optimization strategy based on an orthogonal approach was then implemented using the JMP® 17 software. Library A was designed as an optimal mixture design comprising nine mRNA-LNP formulations, including one center point, to explore the compositional space of four lipid components. The molar ratios were varied as follows: SM-102 (20.0–50.0 %), DSPC (10.0–59.9 %), and cholesterol (19.0–38.5 %), while DMG-PEG2000 content was maintained constant at 1.5 %. Based on experimental performance metrics from Library A, a second formulation set, namely Library B, was generated with refined constraints to further narrow the search space and enhance delivery efficiency. This iterative design enabled targeted exploration of lipid ratios, guiding the selection of high-performing CRISPR/Cas9-LNPs with improved transfection outcomes and desirable physicochemical characteristics.

CRISPR/Cas9-loaded LNPs were prepared using the lipid compositions identified as top-performing in the preceding optimization workflow. To further enhance delivery performance, the *w*/w ratios between Cas9 mRNA and sgRNA were optimized by varying across a new subset of formulations. This allowed fine-tuning of the RNA stoichiometry to maximize physicochemical characteristics, gene-editing activity, and downstream signaling. Final formulations were selected based on their ability to induce robust *in vitro* indel formation while maintaining particle stability and reproducibility.

2.2.3. Physicochemical characterization

2.2.3.1. Particle size and zeta potential measurements. Hydrodynamic diameter, PDI, and zeta-potential were measured using a Zetasizer Advance Ultra (Malvern Instruments, UK) at 25 °C. For size and PDI measurements, samples were placed directly into disposable cuvettes and analyzed at a backscattering angle of 173° under ambient conditions. Zeta-potential measurements were conducted following a 1:8 dilution with highly purified water (HPW). Nanoparticle tracking analysis (NTA) was performed using a Nanosight Pro (Malvern Instruments, UK). LNPs were diluted in PBS to fall within the manufacturer's recommended concentration range. For each sample, three 60-s videos were recorded at 25 °C using a syringe pump set to the arbitrary unit of 20 speed. Video data were processed using optimized detection thresholds to ensure accurate identification and characterization of particle size populations.

2.2.3.2. Encapsulation efficiency. Encapsulation efficiency was quantified using a modified Quant-it™ RiboGreen (Thermo Fisher Scientific, Darmstadt, Germany) assay [31]. To account for differences in fluorescence signal due to detergent, two independent calibration curves were prepared by diluting eGFP mRNA or a Cas9 mRNA and sgRNA mixture (1:1 *w*/w) in either TE buffer or 2 % Triton X-100 in TE buffer, each at a total RNA concentration of 10 ng/µl. Serial dilutions were performed to obtain RNA concentrations within a range of 5 to 0.3 ng/µl. In a black, flat-bottom 384-well microplate (Greiner Bio One, Kremsmünster, Austria), 5 µl of each calibration standard was added in duplicate and diluted with an equal volume of the corresponding solvent. Blanks were

prepared by adding 10 µl of 1 % TE buffer and 10 µl of 2 % Triton™ X-100 in separate wells. CRISPR/Cas-LNP samples were prepared in duplicates and diluted with either TE buffer (to measure unencapsulated RNA) or 2 % Triton X-100 (to lyse nanoparticles and release total RNA), yielding a final volume of 10 µl per well. The plate was sealed and incubated at 37 °C for 60 min with shaking at 240 rpm. Subsequently, 10 µl of RiboGreen reagent diluted 1:100 in TE buffer was added to each well. Following gentle mixing, fluorescence intensity was measured using a plate reader (Tecan Spark, TECAN, Männedorf, Switzerland) at an excitation wavelength of 480 nm and an emission wavelength of 520 nm. The encapsulation efficiency was calculated as follows:

$$EE\ [\%] = \frac{RNA_{tot} - RNA_{unen}}{RNA_{tot}} \times 100$$

where RNA_{tot} represents the total RNA concentration measured in Triton-X-100 buffer wells, and the RNA_{unen} refers to the RNA concentration quantified in TE buffer wells.

2.2.3.3. Morphological evaluation by Cryo-TEM. Particle morphology was assessed using cryogenic transmission electron microscopy (Cryo-TEM). Samples were concentrated using a spin column at 5000 x g for 25 min at 4 °C, resulting in a theoretical lipid concentration of 2.55 mg/ml. As described in [32], 3.5 µl of the concentrated samples were applied to 2 nm pre-coated Qunatifoil R3/3 holey carbon-supported copper grids, followed by vitrification using a Vitrobot Mark IV (Thermo Fisher Sciences). Vitrified samples were imaged at various magnifications using EM-TOOLS (TVIPS GmbH) on a Tecnai G2 Spirit transmission electron microscope (Thermo Fisher Sciences) equipped with a F218 2048 × 2048 pixel CCD camera (TVIPS GmbH) at 120 kV.

2.2.4. Cell culture

H1299 (ATCC: CRL-5803) and A549 (ATCC: CRM-CCL-185) were cultured using RPMI-1640 containing 10 % FBS (Sigma-Aldrich, Taufkirchen, Germany) and 1 % P/S. Hela-eGFP cells (Cell Biolabs: AKR-213) were cultured in DMEM (high glucose) containing 10 % FBS, 0.1 mM MEM NEAA, 2 mM L-glutamine, and 10 µg/ml blasticidin. Calu-3 (ATCC: HTB-55) was cultured in Eagle's MEM containing 10 % FBS. Cells were maintained in 75 cm^2 flasks and subcultured at 37 °C in a humidified atmosphere with 5 % CO_2.

2.2.4.1. mRNA expression. The delivery efficiency of the mRNA-LNPs was examined by monitoring the expression levels of an enhanced green fluorescent protein (eGFP) reporter gene. H1299 and A549 cells were seeded in 24-well plates (Greiner Bio One, Kremsmünster, Austria) at densities of 10,000 and 30,000 cells per well, respectively. After 24 h, triplicate wells were treated with 100 ng of encapsulated eGFP mRNA, and untreated cells served as a blank. Following a 48-h incubation, cells were washed with PBS, detached using 0.05 % trypsin-EDTA, diluted 1:2 with RPMI-1640, and transferred to a centrifuge tube. Samples were centrifuged at 500 x *g* for 5 min, the supernatant was discarded, and the cell pellets were resuspended in PBS. After a second centrifugation step, the pellets were resuspended in PBS containing 2 mM EDTA. An Attune NxT flow cytometry (Thermo Fisher, Germany) was used to measure the median fluorescence intensity (MFI) with excitation at 488 nm and emission detection at 530 nm.

2.2.4.2. eGFP knockout analysis. To assess CRISPR/Cas9-mediated gene knockout efficiency, the reduction in eGFP fluorescence was quantified in HeLa-eGFP reporter cells by flow cytometry. HeLa cells stably expressing an eGFP reporter were seeded in a 24-well plate at a density of 25,000 cells per well. After 24 h, cells were treated in triplicate with 100 ng of encapsulated RNA (Cas9 mRNA and sgRNA mixed at predefined *w*/w ratios). An equivalent amount of RNA mixed with Lipofectamine 2000 (Thermo Fisher Scientific) served as a positive control (PC), while RNA resuspended in Opti-MEM was used as the negative control (NC). Untreated cells were included as a blank. Following a 48-h incubation, cells were washed with PBS, detached using 0.05 % trypsin-EDTA, and diluted 1:2 with RPMI-1640. The suspension was transferred to a centrifuge tube and centrifuged at 500 x *g* for 5 min. After removing the supernatant, cells were resuspended in PBS, centrifuged again, and finally resuspended in PBS containing 2 mM EDTA. The MFI of eGFP was analyzed using an Attune NxT flow cytometry (Thermo Fisher, Germany) with excitation at 488 nm and emission at 530 nm.

2.2.4.3. Evaluation of gene editing efficiency. To confirm CRISPR/Cas9-mediated gene editing, complementary methodologies were employed. Unless otherwise stated, A549 cells were seeded in a 24-well plate at a density of 30,000 cells per well. After 24 h, the cells were transfected with 240 ng of total encapsulated RNA, consisting of Cas9 mRNA and sgRNA mixed at pre-defined *w*/w ratios. As a PC, Lipofectamine 2000 (Thermo Fisher Scientific) complexed with Cas9 mRNA and sgRNA at the same total RNA concentration was used. For the NC, Cas9 mRNA and sgRNA were diluted in Opti-MEM without any transfection reagent. All treatments were performed in triplicate under identical conditions. Following a 48-h incubation, the cells were harvested, and genomic DNA was extracted using the DNeasy blood & tissue kit (Qiagen, Venlo, Netherlands), according to the manufacturer's protocol.

2.2.4.3.1. Droplet digital PCR (ddPCR). ddPCR was employed to precisely quantify gene editing events at the target locus. Each reaction was prepared using 2× ddPCR Supermix for Probes (no dUTP), supplemented with primers at a final concentration of 900 nM, FAM- or HEX-labeled probes at 250 nM, and *Hin*dIII restriction enzyme to facilitate template digestion. The template DNA (100 ng per reaction) was added to reach a total volume of 20 µl. The reaction mixtures were loaded into a droplet generation cartridge along with droplet generation oil, and droplets were formed using the QX200™ Droplet Generator (Bio-Rad). The resulting emulsions were transferred to a 96-well plate and sealed for thermal cycling. PCR amplification was performed under the following conditions: initial denaturation at 95 °C for 10 min, followed by 40 cycles of denaturation at 94 °C for 30 s, and annealing/extension at 55 °C for 6 min. A final extension was carried out at 98 °C for 10 min, followed by a hold at 4 °C. After amplification, droplets were analyzed using the QX200™ Droplet reader (Bio-Rad), and fluorescence signals were quantified using the QuantaSoft™ Analysis Pro software.

2.2.4.3.2. Sanger sequencing. Sanger sequencing was used as a complementary approach to ddPCR to detect indels at the target locus. To visualize the gene sequence following CRISPR-mediated editing, PCR was performed using primers flanking the target site, designed to amplify a ~ 500 bp region spanning the expected cleavage site. PCR amplification was performed using the Phusion Hot Start II High-Fidelity PCR Mastermix. The following cycling conditions were employed: initial denaturation at 98 °C for 10 s, 35 cycles of additional denaturation at 98 °C for 10 s, annealing at 61.5 °C for 30 s, extension at 72 °C for 30 s, followed by a final extension at 72 °C for 10 min. The PCR products were verified by electrophoresis on a 1 % agarose gel and subsequently purified using ExoSAP-IT Express PCR Product Cleanup Reagent. Purified amplicons were subjected to Sanger sequencing, and the gene editing efficiency was analyzed using the ICE CRISPR analysis tool [33].

2.2.4.3.3. T7 endonuclease I (T7EI) assay. The T7EI was employed as an additional method for detecting CRISPR/Cas9-induced indels by cleaving mismatched DNA heteroduplexes formed during reannealing of PCR-amplified target sequences. A549 cells were seeded in a 24-well plate at a density of 30,000 cells per well. After 24 h, the cells were treated with 50–150 ng of encapsulated RNA containing Cas9 mRNA and sgRNA mixed at predefined *w*/w ratios. Following a 48-h incubation, cells were washed with PBS, detached using 0.05 % trypsin-EDTA, diluted 1:2 with RPMI-1640, and transferred to a centrifuge tube. Samples were centrifuged at 500 x *g* for 5 min, and the supernatant was discarded. The assay was conducted using the GeneArt™ Genomic Cleavage Detection Kit, following the manufacturer's instructions. The

cell pellet was lysed using the provided lysis buffer and proteinase K. After lysis, the *KRAS* sequences were amplified using the kit's supplied reagents and primers. The resulting amplicons were denatured and reannealed to form heteroduplexes, which were then digested with the detection enzyme to identify indels introduced by CRISPR/Cas9 activity. For the NC, the cleavage enzyme was replaced with RNase-free water to confirm the background signal. Cleaved products were resolved on a 1.25 % agarose gel with 1× SYBR® Gold. Using a ChemiDoc (Bio-Rad) imaging system, the gel bands were visualized.

2.2.4.4. Transport under mucin-producing conditions. To assess the ability of the optimized CRISPR/Cas9-LNPs to traverse the mucus barrier and achieve cellular uptake under mucin-producing conditions following pulmonary administration, a transport assay was carried out. Calu-3 cells were cultured and transfected at the air-liquid interface (ALI) using Transwell™ inserts (Corning™, NY, USA). Basolateral chambers were filled with 700 µl supplemented Eagle's MEM. The apical chamber was seeded with 100 µl of a single-cell suspension at 2.5×10^5 cells per insert. After 72 h, the ALI was established by aspirating the apical medium. The basolateral medium was then replaced with Pneuma-Cult™ ALI medium (STEMcell Technology, Vancouver, Canada), which was exchanged twice at 48-h intervals. Transfection was performed seven days after the airlift. LNPs were formulated using 80 % Cas9 mRNA and 20 % Alexa Fluor™ 647-labeled eGFP mRNA, and the sgRNA, following the microfluidic protocol described in Section 2.2.1. As a PC, Lipofectamine 2000 (Thermo Fisher Scientific) was complexed with the same RNA mixture (80 % Cas9 mRNA, 20 % labeled eGFP mRNA) and sgRNA at an equivalent total RNA concentration. For the NC, the same RNA mixture was diluted in Opti-MEM without any transfection reagent. The formulation was applied apically, and cultures were incubated for 24 h. For staining, Hoechst 33342 stock (10 mg/ml in HPW) was diluted 1:200 in PBS and added basolaterally (400 µl). Apically, 100 µl of Hoechst (1:200) and AF488-WGA (1:100) was applied. Following a 15-min incubation at 37 °C, the staining solution was removed, and the apical side was washed twice with 50 µl PBS. Basolaterally, inserts were transferred sequentially through three wells containing 400 µl PBS each. Membranes were excised, mounted on coverslips using FluorSave™ (Merck, Darmstadt, Germany), and imaged using 40× and 63× oil-immersion objectives on a SP8 inverted confocal laser scanning microscope (Leica, Wetzlar, Germany).

2.2.4.5. Cytotoxicity. The Cell Counting Kit-8 (CCK-8) assay was used to evaluate the cytotoxicity and viability of the cells following treatment with CRISPR/Cas9-LNPs. A549 cells were seeded in 96-well plates at a density of 5,000 cells per well. Following a 24-h incubation, the cells were transfected with CRISPR/Cas9-LNPs containing total RNA, composed of a mixture of Cas9 mRNA and negative control sgRNA at predetermined *w*/w ratios, across a concentration range of 10 to 80 ng per well. This range corresponds to the effective working concentration, taking into account the adjusted cell density to ensure consistent RNA exposure per well. Untreated cells were included as blank controls. After 48 h, 5 µl of CCK-8 solution was added to each well, followed by another 4-h incubation at 37 °C. The absorbance of each well was measured at 450 nm using a Tecan Spark (Männedorf, Switzerland) plate reader. The cell viability (%) was quantified based on the metabolic activity of viable cells, according to the following equation:

$$Viability\ [\%] = \frac{Abs_{sample} - Abs_{media}}{Abs_{blank} - Abs_{media}} \times 100$$

where Abs_{sample} is the absorbance of the wells transfected with LNPs, Abs_{media} refers to the absorbance of wells containing only culturing medium, and Abs_{blank} denotes the absorbance of wells containing both cells and culturing medium.

2.2.4.6. Cell apoptosis assay. To investigate the cellular response to CRISPR/Cas9-LNP transfection, apoptosis and necrosis were evaluated with Annexin V and PI staining followed by flow cytometry analysis. A549 cells were seeded in a 12-well plate at a density of 100,000 cells per well and incubated for 24 h. Cells were then transfected with CRISPR/Cas9-loaded LNPs containing total RNA, composed of Cas9 mRNA and sgRNA mixed at predetermined *w*/w ratios, at a final concentration of 500 ng per well. Following 48 h of incubation, the cells were harvested, washed twice with PBS, and adjusted to 1×10^6 cells/ml using the Annexin-binding buffer. Subsequently, 10 µl of AF488-Annexin V and 1 µl of PI were added to 100 µl aliquots of the cell suspension. After a 15-min incubation in the dark, the aliquots were further diluted with 400 µl Annexin-binding buffer and vortexed. Fluorescence signals were measured using a flow cytometer, and data were analyzed to distinguish live, apoptotic, and necrotic cell populations based on Annexin V and PI staining profiles.

2.2.5. In vivo studies

All animal experiments in this study were conducted in full compliance with Spanish and European regulations (Royal Decree 53/2013 and Directive 2010/63/EU), under authorization from the competent authority (Xunta de Galicia, project ID #15012/2023/007). Ethical approval was obtained following a mandatory positive evaluation by the Bioethics Committee of the University of Santiago de Compostela. All procedures adhered to the principles of the Three Rs (Replacement, Reduction, and Refinement) in animal research.

2.2.5.1. Repeated-dose safety evaluation. To assess the safety profile of two lead formulations designed for CRISPR/Cas9 delivery, a short-term repeated-dose safety study was carried out in healthy mice. Briefly, seven-week-old female Swiss mice weighing approximately 20 g were randomly assigned to four groups: PBS, LNP NC, A6 3:1, and A8 1:1 ($n = 3$ animals per group). The LNP NC group received a formulation matching the lipid composition and Cas9 mRNA/sgRNA *w*/w ratio of LNP A6, but with a scrambled sgRNA sequence serving as a non-targeting negative control. Each formulation was administered intratracheally at a dose of 0.3 mg/kg in a volume of 50 µl, twice weekly for two weeks. The animals were clinically observed for 30 min following each administration, and body weights were recorded twice a week. Clinical signs were monitored throughout the study using a standardized scoring system to assess fur condition, respiratory rate, behavior, and posture. On day 14 after the first dose, mice were euthanized, and blood samples were collected to evaluate potential systemic toxicity. Hematological analysis was performed using a Mindray BC5000-Vet analyzer, while serum samples were assessed for clinical biochemistry with a VetScan VS2 analyzer (Zoetis) employing the Comprehensive Diagnostic Profile (Zoetis).

2.2.5.2. Efficacy evaluation of CRISPR/Cas9-LNPs in a murine lung tumor model. To assess the therapeutic potential of CRISPR/Cas9-LNPs in a physiologically relevant setting, we employed an orthotopic lung cancer model in immunodeficient mice. Human NSCLC A549 cells expressing luciferase (A549-luc) were injected into the left lung of female NMRI-nude mice (Janvier Laboratories) *via* the intercostal space at a dose of 1×10^6 cells in 50 µl PBS per mouse, following the protocol described by Borrajo et al. [34]. Bioluminescence imaging was performed twice weekly in anesthetized animals using an IVIS Spectrum imaging system (Revity), starting on day 7 post-implantation. Animals were enrolled in the study once the bioluminescent signal exceeded 10^6 (total flux) and showed a consistent increase across two consecutive measurements, indicating successful tumor establishment. Mice were assigned to four experimental groups ($n = 6$ animals per group) to ensure comparable mean luminescence signals and standard deviations across groups. Animals exhibiting bioluminescence signals beyond ±2 standard deviations from the group mean were excluded from the study. Intratracheal administration of 50 µl was performed twice weekly for

three weeks, delivering either formulation A6 3:1 (0.3 mg/kg), formulation A8 1:1 (0.3 mg/kg), LNP negative control (LNP-NC, prepared identically to the formulation used in the toxicity study; 0.3 mg/kg), or PBS. Animals were monitored daily, with body weights recorded and tumor progression assessed twice weekly using the IVIS Spectrum imaging system. At study termination, animals were euthanized, lungs were harvested, and blood was collected for serum isolation and subsequent downstream analyses.

2.2.5.2.1. Cytokine assessment. To assess systemic immune responses, serum samples were collected from NMRI-Nu mice following treatment and from untreated controls. Concentrations of key cytokines such as IFN-γ, TNF-α, IL-6, and IL-10 were measured using a multiplex bead-based immunoassay (LEGENDplex™ Mouse Th Cytokine Panel, BioLegend; Cat#741044), performed according to the manufacturer's protocol.

2.2.5.2.2. Histological analysis of murine lungs post-treatment. Lung tissue was harvested from 8 mice (2 per group). Immediately after excision, the lungs were gently inflated with 4 % paraformaldehyde (PFA) in PBS and subsequently immersion-fixed in the same fixative for 24 h at 4 °C. After fixation, tissues were dehydrated through a graded ethanol series, cleared in xylene, and embedded in paraffin. Paraffin-embedded lung tissues of 1 animal per group were sectioned at 5 μm thickness using a microtome and mounted on Superfrost glass slides. For general histological evaluation, four consecutive sections per animal were stained with hematoxylin and eosin (H&E, Morphisto, Germany). To assess extracellular matrix composition and connective tissue structures, Azan staining (Morphisto, Germany) was performed. Periodic Acid-Schiff (PAS, Morphisto, Germany) staining was used to visualize polysaccharides and glycoproteins. For the detection of apoptotic cells, the terminal deoxynucleotidyl transferase dUTP nick end labeling (TUNEL) assay was carried out using a commercial *in situ* cell death detection kit (HRP-DAB ab206386, Abcam) according to the manufacturer's instructions. All stained sections were dehydrated, coverslipped with mounting medium, and imaged using a brightfield microscope (Axiolab 5, Zeiss, Germany) and a digital camera setup (Axiocam 208 color, Zeiss, Germany). Image analyses were performed using ZEN software (Zeiss, Germany). Apoptotic cells were quantified by calculating the density of TUNEL-positive cells, defined as the number of TUNEL-positive cells divided by the area of the tumor section. Quantification was performed across $n = 8$ sections per group.

2.2.6. Statistics

Unless otherwise stated, all experiments were performed in triplicate, and the results are presented as the mean ± standard deviation. All statistical analysis was performed using GraphPad Prism (GraphPad Software, USA).

3. Results and discussion

3.1. Formulation development and optimization

To address the poor druggability and frequent resistance associated with *KRAS* mutations, this study leveraged the high therapeutic potential of CRISPR/Cas9 systems. However, the limited number of clinical trials involving CRISPR/Cas9 highlights the challenge of achieving efficient and safe delivery. This hurdle is even more pronounced for non-viral platforms targeting extrahepatic tissues, such as the lung. To overcome these barriers, we implemented an optimization strategy using eGFP mRNA-LNPs as a surrogate to rapidly evaluate transfection efficiency and physicochemical properties across diverse lipid compositions. This approach, supported by recent studies validating the predictive value of mRNA surrogates for CRISPR delivery [35], enabled rational formulation design through orthogonal mixture modeling. Iterative refinement led to the identification of lead formulations with enhanced gene editing activity and favorable biocompatibility, establishing the platform for *in vivo* validation.

Current FDA-approved LNPs are optimized for hepatic transfection, requiring re-engineering for efficient transfection in other tissues such as the lungs. Given their established safety and clinical efficacy, we selected these lipid components and varied their lipid molar ratios to enhance delivery to pulmonary cells (Fig. 1A). Specifically, the ionizable lipid SM-102 content was adjusted between 20.0 mol% and 50.0 mol%, cholesterol between 19.0 mol% and 38.0 mol%, and DSPC between 10.0 mol% and 59.5 mol%. The N/P ratio and DMG-PEG2000 lipid content were fixed at 6 and 1.5 mol%, respectively, for all formulations. Formulation A2 replicated the composition of Moderna's Spikevax vaccine, serving as a clinically relevant benchmark for comparison. LNPs encapsulating eGFP mRNA with varied lipid molar ratios were prepared (Fig. 1A, Library A1 - A9) and allowed for the rapid and quantitative assessment of transfection efficiency. Based on initial screening results from Library A, a refined subset (Library B) was set up to further investigate promising compositions. Remarkably, formulations A6 and A8 demonstrated nearly 10-fold higher MFI in H1299 cells, an NSCLC cell line, compared to the benchmark A2 (Fig. 1B). This is in agreement with previous findings, emphasizing the necessity of tissue-specific formulation optimization to ensure efficient transfection [36]. Interestingly, formulations of library B did not surpass the performance of A6 and A8, suggesting a plateau of effectiveness within the tested compositional space.

All formulations met critical quality attributes, with hydrodynamic diameters below 120 nm and PDI under 0.2 (Fig. 1C). Similarly, the ζ-potential measurements revealed near-neutral surface charges, indicative of favorable tolerability (Fig. S1), and encapsulation efficiencies remained uniformly high (Fig. 1D). Notably, the most effective formulations contained substantially lower amounts of ionizable lipid than the benchmark formulation (A2). This was unexpected, given the central role of ionizable lipid in facilitating endosomal escape, often considered the main bottleneck in mRNA delivery [37,38]. The reduced SM-102 content may also confer an immunological advantage of minimizing the overall immunogenicity of the formulation [39]. Collectively, these results indicate that while physicochemical properties remain largely unchanged across lipid ratios (excluding PEGylated lipids), transfection efficiency is highly sensitive to compositional tuning.

Based on the initial screening, formulations A6 and A8 were selected for further evaluation and loaded with Cas9 mRNA and sgRNA at a 3:1 (*w*/w) ratio. Their physicochemical properties were then compared to their respective eGFP-loaded counterparts. Formulation A6 showed no significant differences in hydrodynamic diameter, while formulation A8 presented a modest increase. Despite this variation, both formulations remained within the critical quality attribute specifications for LNPs and are expected to remain suitable for pulmonary delivery, as particle size alone does not fully determine deposition efficiency (Fig. 1E). Both formulations maintained low PDI (< 0.2) and near-neutral ζ-potentials, regardless of payload (Fig. 1E and Fig. 1G). Similarly, no significant differences in the encapsulation efficiency of both Cas9 mRNA/sgRNA were identified (Fig. 1F). These results indicate the RNA payload can be interchanged without compromising the physicochemical properties of the delivery system. The capacity of the formulation to co-encapsulate both RNA species offers an advantage over adeno-associated viral vectors, which are constrained by their limited packaging capacity (~4.7 kb) and therefore often require sgRNA to be delivered separately [40]. Polymeric nanoparticles have been explored for pulmonary CRISPR delivery but face challenges such as cytotoxicity, mucociliary clearance, and limited transfection efficiency, highlighting the potential of optimized LNPs as a safer and more effective alternative [41]. This modularity is particularly advantageous for clinical translation, as it allows the incorporation of patient-specific sgRNAs into pre-validated LNP platforms, accelerating personalized therapeutic development.

3.2. Optimization of Cas9 mRNA/sgRNA LNPs

Based on the optimized lipid compositions identified in Fig. 1 and the

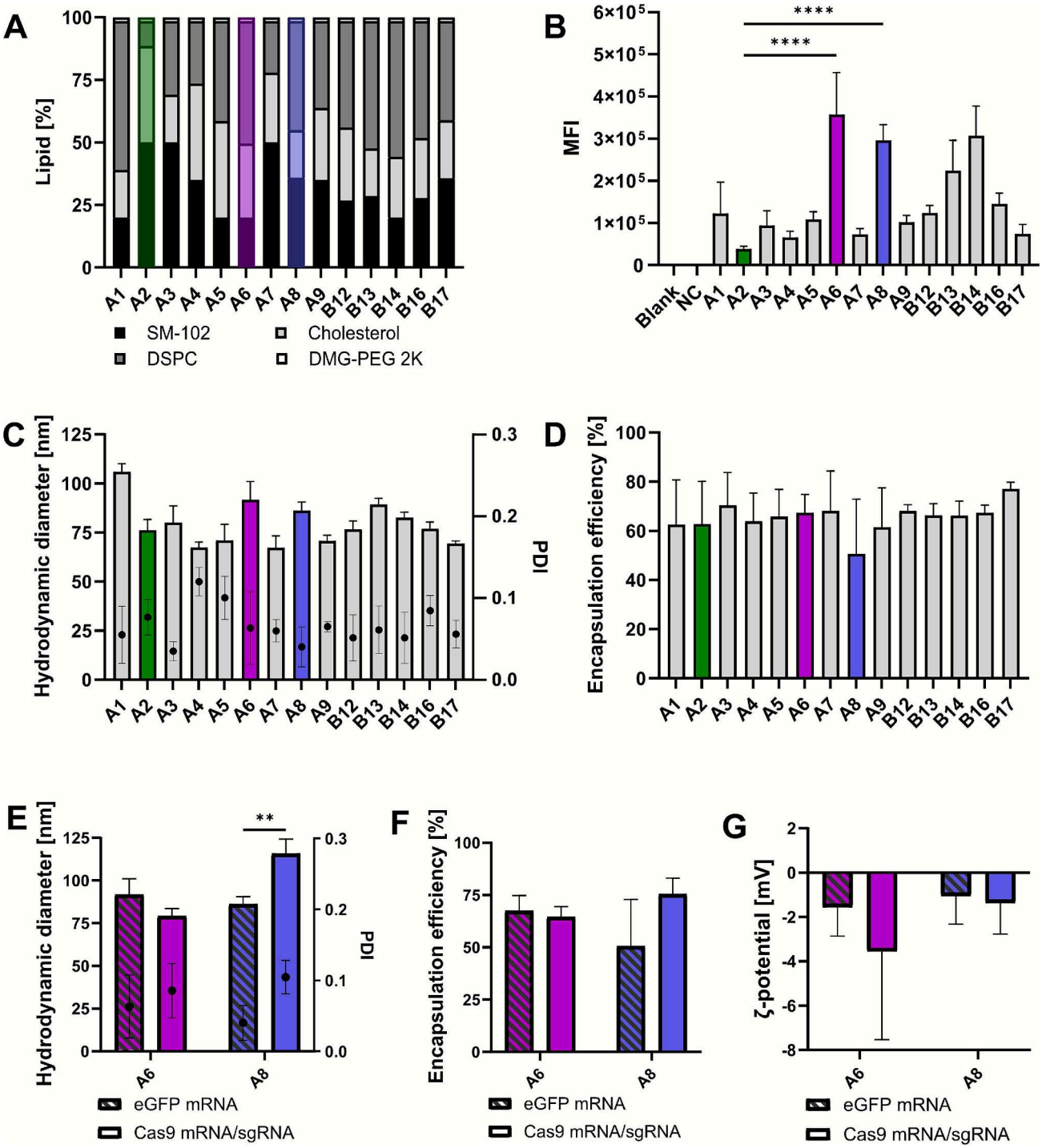

Fig. 1. Characterization of two mRNA LNP libraries (A and B) with varied lipid compositions and subsequent preparation of Cas9 mRNA/sgRNA -LNPs. **A)** Lipid composition of screened formulations. **B)** eGFP expression of screened formulations in H1299 cells. **C)** Hydrodynamic diameter and PDI. **D)** Encapsulation efficiency. **E - G)** Impact of RNA loading on hydrodynamic diameter, PDI, encapsulation efficiency, and ζ-potential. Statistical analysis: B—D, Ordinary one-way ANOVA with Tukey's multiple comparisons test; *E*-G: two-way ANOVA; $^{**}p < 0.01$, **** $p < 0.0001$. NC: negative control.

optimal physicochemical profile obtained for the lead candidate, we initially assessed formulation A6 for gene editing using the T7EI assay. LNP A6 showed only modest gene editing efficiency (Fig. S2). This outcome encouraged us to explore whether altering the *w*/w ratios of Cas9 mRNA to sgRNA could enhance performance without compromising colloidal stability. Because editing efficiency may also depend on the specific lipid composition, we extended the analysis to include formulation A8, which was identified as an additional lead candidate with a robust physicochemical profile. Therefore, formulations A6 and A8 were selected for further screening across Cas9 mRNA to *KRAS* sgRNA ratios ranging from 1:1 to 10:1.

Physicochemical characterization revealed no significant differences in hydrodynamic diameter, PDI, encapsulation efficiency, or ζ-potential across all tested Cas9 mRNA and sgRNA ratios (Fig. 2A, S3), suggesting that RNA stoichiometry does not substantially influence the physicochemical properties of the LNPs. Comparable particle size measurements for formulations A6 3:1 and A8 1:1 were confirmed using the orthogonal method of NTA (Fig. S4).

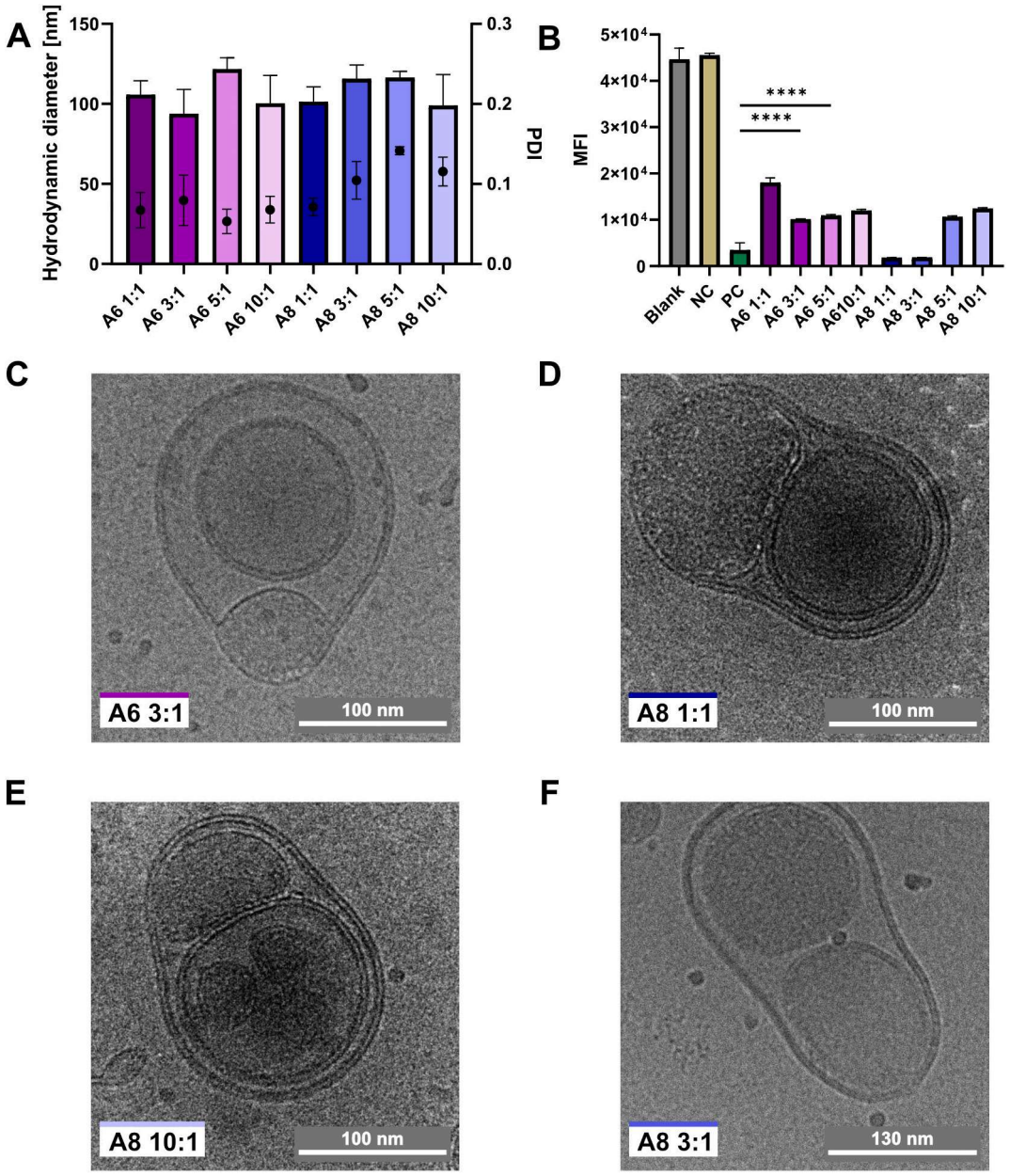

Fig. 2. Physicochemical and functional characterization of CRISPR-LNPs during optimization of Cas9 mRNA/sgRNA *w*/w ratios. **A)** Hydrodynamic diameter and PDI of formulations A6 and A8 at varying mRNA/sgRNA ratios. **B)** eGFP knockout efficiency of A6 and A8 in HeLa-eGFP reporter cells. **C—F)** Cryo-TEM images of A6 and A8 at different mRNA/sgRNA ratios. NC: negative control; PC: positive control. Statistical analysis: Ordinary one-way ANOVA with Tukey's multiple comparisons test; **** $p < 0.0001$.

To initially assess gene knockout efficiency, we employed eGFP-HeLa reporter cell lines, which provide a robust and standardized system for quantifying CRISPR/Cas9 activity. The stable and uniform expression of eGFP in this model enables rapid and sensitive detection of knockout events by flow cytometry, thereby allowing us to benchmark the performance of novel formulations under controlled conditions. This approach ensured reproducibility and facilitated direct comparison with Lipofectamine as a PC. Formulations A8 1:1 and 3:1 achieved the highest knockout levels, comparable to Lipofectamine, with no significant difference between them (Fig. 2B).

These variations in performance may be attributed to differences in LNP morphology. Conventional LNP formulations, such as A2, exhibit an electron-dense core, where lipids and RNA co-localize [42]. However, recent studies have shown that inducing a bleb-like structure (a spherical protrusion attached to the main LNP) can drastically enhance transfection efficiency. This compartment is believed to be enriched in RNA and may improve payload stability and delivery [43]. Blebs can be induced by high-molarity acidic buffers used for RNA dissolution during LNP preparation, which promote the fusion of small positively charged vesicles with RNA-loaded LNPs during dialysis. Upon neutralization, phase separation occurs, with the RNA migrating toward the bleb compartments [43]. Notably, none of the investigated formulations in this study exhibited the canonical electron-dense core morphology usually found in LNP, potentially explaining their superior transfection efficiency compared to A2. Formulation A6 3:1 most closely resembles the bleb structure (Fig. 2C). In contrast, A8 (1:1 and 3:1) showed a divesicular lipid architecture more akin to liposomes (Fig. 2D and F), which may explain their superior performance. Cheng et al. have similarly observed that the induction of liposomal LNPs can increase the transfection efficiency and promote extrahepatic delivery. In their

formulations, a solid core within an aqueous spherical lipid bilayer was observed, depending on the ratio of ionizable lipid to bilayer-forming lipids [44]. Interestingly, formulations A8 at different RNA molar ratios displayed a similar liposomal structure, but with elongated, ellipsoidal vesicular structures. Such ellipsoidal morphology may contribute to the improved transfection efficiency observed, as rod-like geometries are known to enhance cellular internalization in inorganic nanoparticles [45]. Notably, formulation A8 at a 10:1 Cas9 mRNA to sgRNA ratio also exhibits a divesicular structure (Fig. 2E), but one vesicle appeared multivesicular, possibly hindering RNA release and limiting transfection efficiency.

A possible mechanistic explanation for the improved efficiency is the "warhead" theory [44]. According to this model, the lipid-rich domain of the particle interacts with the endosomal membrane, promoting fusion with the liposome. This interaction then facilitates the release of the particle's components into the cytosol. As the adjacent compartment is believed to be rich in mRNA, this fusion event may enable a greater fraction of the payload to reach the cytosol, thereby enhancing expression. This provides a structural rationale for why bleb-like or liposomal morphologies may outperform conventional electron-dense cores. The morphologies observed in the cryo-TEM images may also influence the apparent sizes measured by DLS. DLS assumes spherical particles and calculates the hydrodynamic radius of an equivalent sphere that diffuses at the same rate. For nonspherical particles, this results in biased estimates, with intensity-weighted measurements skewed toward larger diameters [46,47]. A similar limitation applies to NTA, which also reports sphere-equivalent hydrodynamic diameters derived from translational diffusion. Nonetheless, this does not compromise the conclusions presented in this study, as the main objective was to identify particles below 120 nm, which remains valid even if the sizes are slightly overestimated.

3.3. *In vitro evaluation of optimized Cas9 mRNA/sgRNA LNPs*

Following optimization of the Cas9 mRNA/sgRNA w/w ratios, we next assessed the *in vitro* gene editing efficiency of selected formulations using high-precision quantification techniques, evaluated cytotoxicity, examined the impact on downstream cellular signaling, and analyzed their ability to penetrate mucus. These studies aimed to validate the therapeutic potential of the LNPs prior to *in vivo* application.

3.3.1. *Gene editing*

Based on the gene knockout results (Fig. 2B), formulations A6 (3:1 and 5:1) and A8 (1:1 and 3:1) were selected for further evaluation in A549 cells, which harbor the *KRAS* G12S mutation. Unlike HeLa, A549 cells more closely represent the target pulmonary tissue. However, the absence of a readily detectable reporter gene requires the use of more sophisticated detection methods, which in turn reduces experimental throughput. ddPCR analysis revealed that formulations A6 3:1, 5:1, and A8 3:1 achieved gene editing efficiencies of approximately 60 %, while A8 1:1 reached nearly 90 %, with no statistically significant difference to Lipofectamine (PC) (Fig. 3A). These results are notable when compared with previous studies employing viral vectors or adenoviral CRISPR systems targeting *KRAS* G12S, which reported tumor suppression of approximately 77 % in A549 cells but required invasive delivery and showed limited editing specificity [48]. Additionally, viral vectors carry the undesired risk of integrating into the host genome at sites of DNA breakage, whereas mRNA-based delivery systems remain confined to the cytosol [49]. Our LNP-based approach achieved comparable or superior editing efficiency with a non-viral, biocompatible platform.

The marked difference in editing efficiencies between formulations A8 1:1 and A8 3:1, yielding approximately 90 % and 60 % gene editing, respectively, highlights the critical role of RNA stoichiometry in determining CRISPR/Cas9-LNP performance. As both formulations were evaluated in the same cell line, these differences cannot be attributed to cell-specific metabolic activity but rather suggest that imbalances in the availability of Cas9 mRNA and sgRNA influence the extent of ribonucleoprotein complex formation. An equimolar 1:1 ratio likely ensures sufficient sgRNA to guide all newly synthesized Cas9 proteins, thereby maximizing editing efficiency. In contrast, an excess of Cas9 mRNA at a 3:1 ratio may lead to disproportionate Cas9 expression relative to sgRNA, resulting in incomplete complex formation and reduced functional activity. These findings emphasize that optimal gene editing outcomes require a finely tuned balance between Cas9 mRNA and sgRNA, tailored to the biological context. Importantly, formulation A8 1:1 combines high editing efficiency with a clinically relevant target and a scalable, non-viral delivery platform, establishing a proof-of-concept study while demonstrating its translational potential. The robust performance in A549 cells strongly motivates subsequent *in vivo* evaluation, particularly in pulmonary models of *KRAS* G12S-driven tumors, where therapeutic options remain limited.

To further support the ddPCR-based quantification of gene editing, we performed Sanger sequencing on genomic DNA from transfected A549 cells. The representative chromatogram from the lead formulation (A8 1:1) showed overlapping and diminished peak intensities in the edited sequence compared to the unedited control (Fig. 3B). These features are consistent with mixed alleles resulting from CRISPR-induced indels, providing qualitative confirmation of successful gene editing. While not used for primary quantification, this sequencing data serves as an orthogonal method that complements the ddPCR findings and supports the presence of on-target genomic disruption.

3.3.2. *Cytotoxicity*

To mitigate potential *in vivo* liabilities, further *in vitro* experiments were conducted, beginning with a cytotoxicity profile. Although the lipid components used in formulations A6 and A8 are FDA-approved and widely regarded as safe [19], formulation-specific effects on cell viability can vary depending on lipid ratios, total lipid dose, and ionizable lipid content [50,51]. Ionizable lipids, while essential for RNA complexation and endosomal escape, can contribute to membrane destabilization and inflammatory signaling if present at high concentrations [52]. Therefore, evaluating the cytotoxicity of newly optimized formulations is critical, especially when modifying the molar ratios of ionizable lipids. A CCK-8 assay was performed to investigate cell viability in A549 cells treated with the Cas9 mRNA-loaded A6 and A8 formulations containing an NC sgRNA. Both formulations maintained high cell viability across all tested doses, with only a modest dose-dependent reduction. Even at the highest dose, cell viability remained above 80 % (Fig. 3C), indicating good tolerability. This provides a direct advantage over permanently cationic polymeric systems, which often induce cytotoxicity through nonspecific electrostatic interactions and membrane destabilization [53]. These findings confirm that our lead formulations not only demonstrate potent gene editing activity but also maintain a favorable safety profile *in vitro*.

3.3.3. *Apoptosis*

KRAS is a central regulator of multiple downstream pathways that control cell proliferation, survival, and apoptosis. Oncogenic *KRAS* mutations, such as G12S, confer constitutive activation of these signaling cascades, promoting tumor growth and resistance to cell death [54]. Therefore, it is essential not only to achieve efficient gene editing of mutant *KRAS* but also to confirm that such disruption translates into functional consequences, particularly apoptosis, which is a key therapeutic goal in cancer treatment. To assess whether *KRAS* editing induced apoptosis, we performed an Annexin V/propidium iodide (PI) double staining assay in A549 cells transfected with our optimized LNP formulations (Fig. 3D). No apoptosis was detected in the untreated control (blank), while the PC (Lipofectamine 2000) showed a measurable increase. Importantly, both A6 3:1 and A8 1:1 formulations showed clear apoptotic responses, exceeding those observed in the PC by nearly 3.7 and 3.6-fold, respectively. These results suggest that our formulations not only achieve gene editing but also trigger downstream cell death

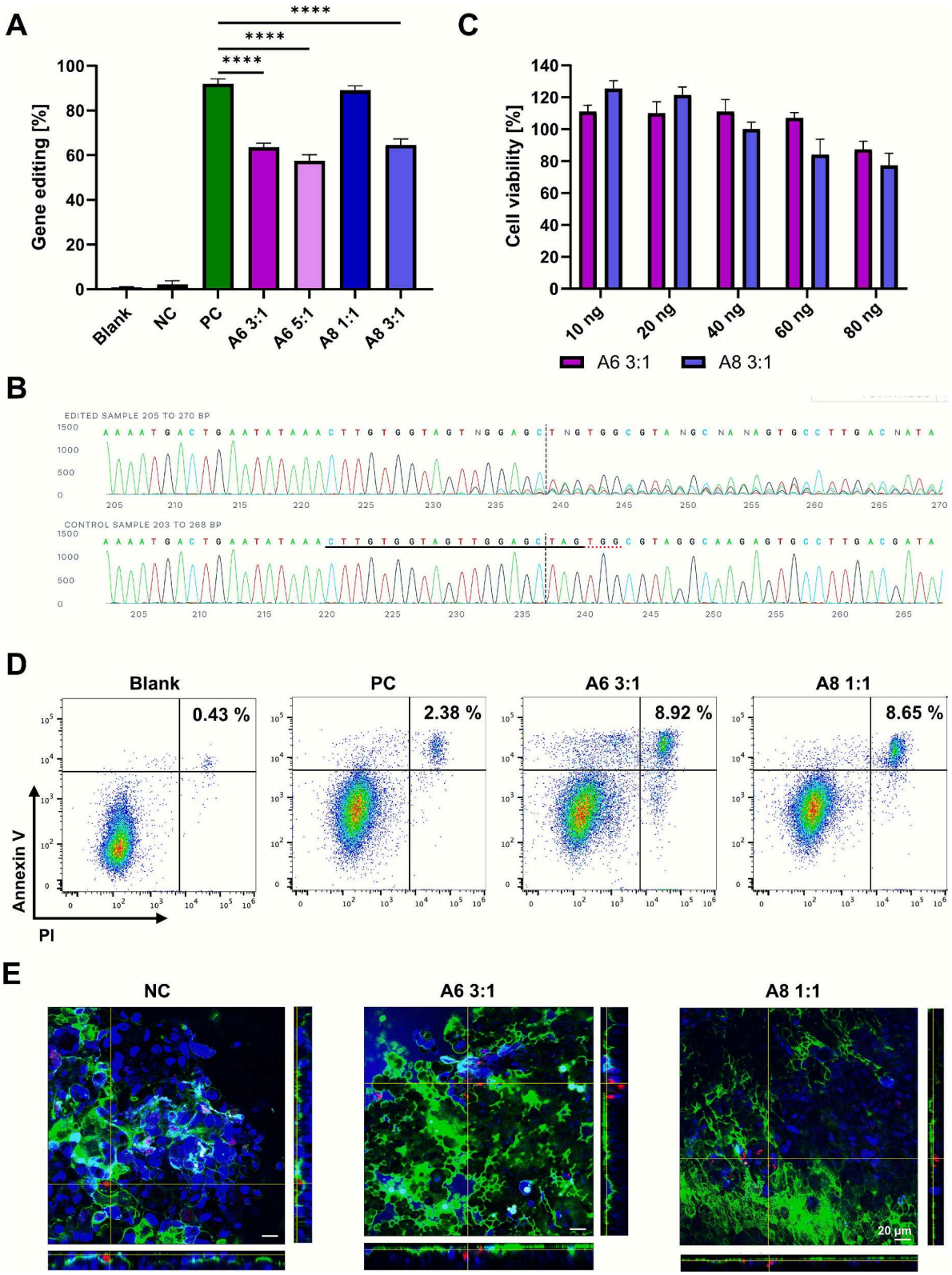

Fig. 3. *In vitro* evaluation of optimized Cas9 mRNA/sgRNA LNPs. **A)** Gene editing analysis by ddPCR of LNPs A6 and A8 at different mRNA/sgRNA ratios. **B)** Gene editing evaluation by Sanger sequencing of formulation A8 1:1 in A549 cells. **C)** Cell viability of A549 cells treated with formulations A6 3:1 and A8 1:1. **D)** Percentage of cells in late apoptosis, as indicated by dual Annexin V/PI staining. **E)** Confocal microscopy of CRISPR/Cas9-loaded LNP penetration in Calu-3 ALI cultures. NC, A6 3:1, and A8 1:1 formulations were visualized with Alexa Fluor™ 647-labeled mRNA (red). Nuclei were stained with Hoechst 33342 (blue) and mucus with AF488-WGA (green). Statistical analysis: ordinary one-way ANOVA with Tukey's multiple comparisons test; **** $p < 0.0001$. NC: negative control; PC: positive control. (For interpretation of the references to color in this figure legend, the reader is referred to the web version of this article.)

pathways, consistent with the therapeutic intent of *KRAS* disruption.

Interestingly, ddPCR analysis (Fig. 3A) showed similar or higher editing values in the PC compared to the LNP-transfected groups, while apoptosis was significantly more pronounced in the latter. This discrepancy may be attributed to differences in the delivery systems. Lipofectamine, composed of cationic and helper lipids, is known to activate inflammatory signaling pathways such as NF-κB, which can modulate cell stress responses and alter cell-death outcomes independently of gene editing [55]. Cationic lipids are particularly prone to disrupting cellular membranes and indirectly triggering innate immune sensors such as Toll-like receptors and RIG-I-like receptors, which can initiate pyroptosis, necroptosis, or other non-apoptotic death modes [56]. These mechanisms can confound the interpretation of gene editing outcomes, as elevated cell death may reflect inflammatory toxicity rather than on-target disruption of *KRAS*. In contrast, our LNP formulations, which were designed with near-neutral surface charge and optimized lipid ratios, appear to induce apoptosis through direct genetic targeting, as evidenced by Annexin V/PI staining and the absence of clear inflammatory effects.

3.3.4. Transport under mucin-producing conditions

Efficient transport and cell uptake in the presence of mucus is a critical prerequisite for LNP formulations intended for pulmonary and local delivery. The respiratory tract is lined with a dense mucus barrier that can impede nanoparticle diffusion and limit therapeutic efficacy. Given the inherent liver tropism of LNPs, direct pulmonary administration *via* intratracheal instillation was employed in the subsequent *in vivo* studies to bypass systemic distribution and target the lungs more precisely. To assess the mucosal penetrative and cell uptake properties of the formulations, the lead candidates A6 3:1 and A8 1:1 were transfected into Calu-3 cells, a mucin-producing epithelial model widely used for evaluating airway drug delivery. This model was chosen over A549 because Calu-3 cells form a multilayered epithelium with enhanced barrier function, thereby providing a physiologically relevant system for assessing nanoparticle transport and cell uptake in a mucin-rich environment. In contrast, A549 cells were reserved for gene editing experiments, as they harbor the *KRAS G12S* mutation and more closely represent the disease-relevant pulmonary cancer context used in our *in vivo* studies [57,58]. For visualization, 20 % of the encapsulated Cas9 mRNA was replaced with red-fluorescing AF647-mRNA, mucin was stained with green-fluorescing AF488, and nuclei with blue Hoechst 33342. We acknowledge that AF488-WGA staining is not selective for secretory mucins, but it nonetheless highlights glycoprotein-rich domains relevant for nanoparticle interactions. Although a continuous mucus layer was not observed, the presence of mucus regions still influenced nanoparticle behavior by facilitating surface interactions. Orthogonal views from confocal imaging revealed co-localization of mRNA with mucus in the NC (Fig. 3E). This co-localization is expected, as the negatively charged RNA was simply dissolved in Opti-MEM and lacks the physicochemical properties required to overcome mucus and cell uptake barriers. Without a protective or penetrating delivery system, the RNA remains trapped, unable to reach the underlying epithelium, demonstrating the importance of the Calu-3 barrier model for evaluating LNP performance.

In contrast, both formulations (A6 3:1 and A8 1:1) exhibited strong mRNA signal at the cellular level, indicating successful transport through mucins and cellular uptake by the Calu-3 epithelium. These observations highlight the importance of tailored delivery systems that are specifically engineered to navigate biological barriers such as mucus, while also demonstrating the utility of the Calu-3 multilayered epithelial model as a physiologically relevant platform for assessing nanoparticle transport and cell uptake. The near-neutral surface charge and PEGylation of the LNPs likely minimized nonspecific interactions with glycoprotein-rich mucus regions and facilitated subsequent cellular entry [29], preliminarily indicating the potential to overcome key physiological challenges. These results should be interpreted as an initial indication of LNP behavior in a mucin-producing system, with further validation planned in more physiologically relevant models, including nebulized and spray-dried LNP formulations.

3.4. In vivo studies

Based on the *in vitro* evaluation and the selection of lead Cas9 mRNA/sgRNA-LNP formulations, we proceeded to *in vivo* validation in healthy and lung tumor-bearing mouse models. This allowed us to investigate the safety profile, delivery efficiency, and therapeutic impact of the system under physiologically relevant conditions. Formulations A6 3:1, A8 1:1, and the LNP-NC were prepared using impingement jet mixing and subsequently concentrated. The physicochemical properties of these batches remained consistent with those produced *via* syringe pump, exhibiting particle sizes below 120 nm, PDI under 0.2, and encapsulation efficiencies exceeding 80 % across all LNPs (Fig. S5).

3.4.1. Safety assessment of formulations

First, a short-term repeated-dose safety study was conducted in healthy Swiss mice to assess the tolerability of the best-performing Cas9 mRNA/sgRNA-LNPs, A6 3:1 and A8 1:1. No mortality or clinical signs of toxicity were observed in any groups following administrations during the experimental period. The animals consistently received the lowest clinical severity scores, as vital and critical clinical signs like respiratory function, behavior, and posture remained within normal parameters throughout the study. Body weight followed a gradual increase trend across all groups (Fig. 4A), indicating overall good health with preserved appetite. At the end of the experiment, mice were sacrificed, and serum was collected for additional analysis. Serum biochemistry revealed no significant alterations in hepatic, pancreatic, or renal markers for the animals treated with both LNPs A6 3:1 and A8 1:1 (Fig. 4B and C), suggesting a well-tolerated systemic safety profile. The hematological profile further supported this assumption. Parameters, including leukocyte, erythrocyte, and platelet counts, remained within normal ranges across all groups (Fig. 4D). Besides, no evidence of bone marrow suppression or systemic hematotoxicity was detected, confirming the good tolerability of the Cas9 mRNA/sgRNA-LNPs. It should be noted that the safety assay was designed to assess tolerability and the absence of systemic adverse effects, rather than to characterize potential local responses, thereby ensuring that the treatment could be advanced with confidence into subsequent efficacy studies.

The absence of systemic toxicity following repeated intratracheal administration of LNPs A6 3:1 and A8 1:1 provides strong evidence that optimized pulmonary delivery of CRISPR/Cas9 can be achieved with a favorable safety profile. This is particularly important given that previous studies have reported acute toxicity associated with certain cationic lipid-based formulations. For instance, DDAB30 LNPs have been shown to induce elevated liver enzymes (alanine aminotransferase (ALT) and aspartate aminotransferase (AST)), increased liver-to-body weight ratios, and histological damage in multiple organs, including the heart and liver, following intratracheal administration [59]. These findings demonstrate the critical importance of rational LNP design to minimize off-target toxicity while preserving delivery efficiency.

As CRISPR-based therapeutics move closer to clinical translation, the development of safe and scalable delivery platforms remains a central challenge. Unlike viral vectors, for instance, which are often limited by immunogenicity and poor tolerability upon repeated dosing, our data demonstrate that optimized Cas9 mRNA/sgRNA-LNPs can be administered intratracheally multiple times without compromising systemic health. This capacity for repeat dosing is especially advantageous in the context of lung cancer, where sustained therapeutic exposure may be required to target heterogeneous tumor populations or address residual disease. By circumventing the immune barriers typically associated with viral delivery, our approach enables a more flexible and safer dosing regimen, expanding the clinical potential of gene editing therapies.

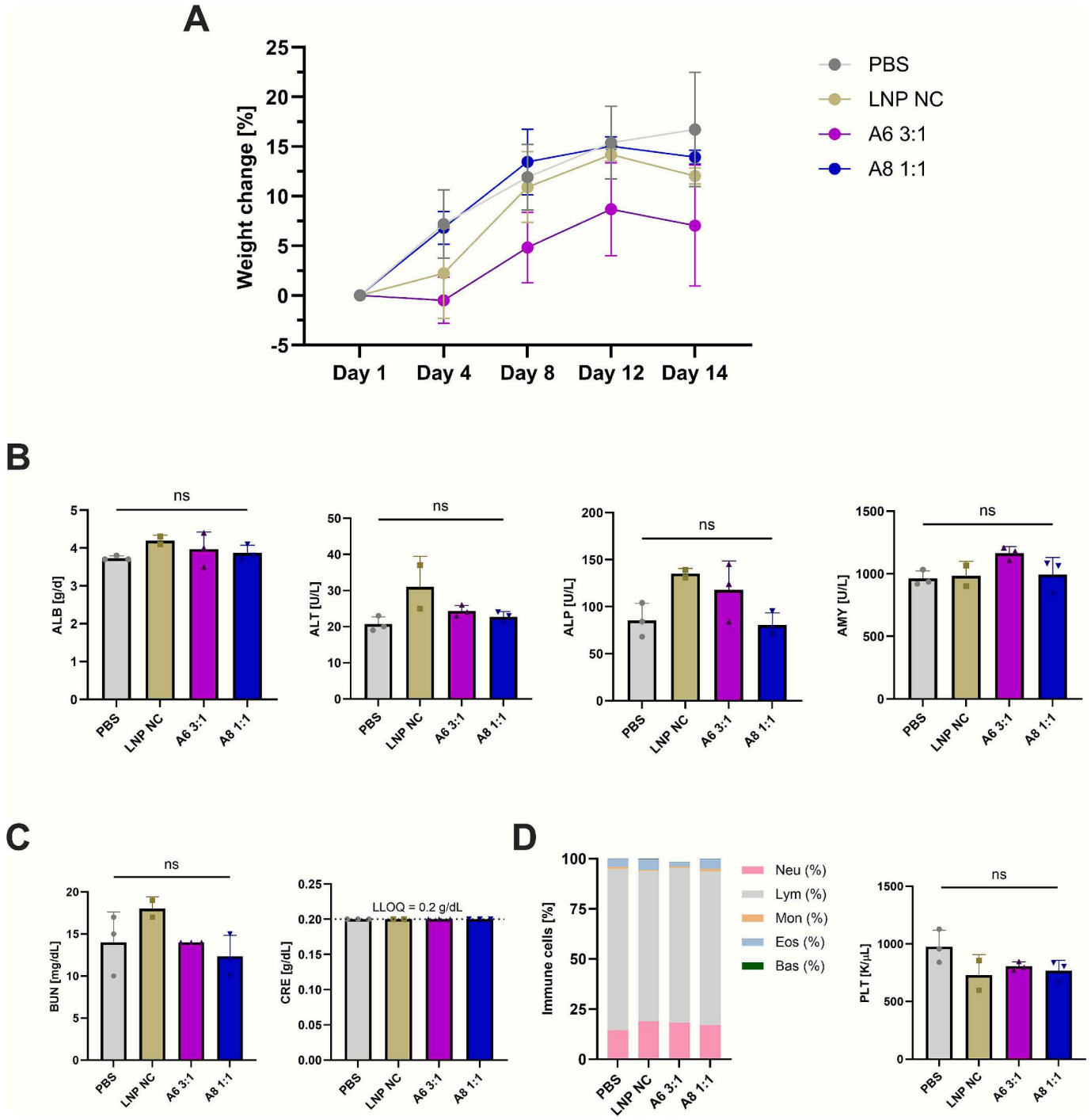

Fig. 4. Serum toxicity assessment of LNPs A6 3:1 and A8 1:1 in healthy mice. Serum samples were collected after administration of formulations and compared to PBS control and LNP NC ($n = 3$ mice per group; $n = 2$ for LNP NC). **A)** Animal body weight change. **B)** Markers of hepatic (albumin (ALB), alanine aminotransferase (ALT), alkaline phosphatase (ALP)), and pancreatic (amylase (AMY)) function. **C)** Kidney function markers: blood urea nitrogen (BUN) and creatinine (CRE). **D)** Relative distribution of circulating immune cell subsets, and platelet counts (PLT). Data are presented as mean ± SD. Statistical significance was determined using one-way ANOVA with Tukey's post-hoc test. ns: not significant compared with PBS for A6 3:1 or A8 1:1.

3.5. *Efficacy evaluation of formulations*

3.5.1. *Establishment of a murine lung cancer tumor model*

To evaluate the therapeutic efficacy of Cas9 mRNA/sgRNA-loaded LNPs, we employed an orthotopic A549 cell xenograft model in immunodeficient mice. These human lung adenocarcinoma cells harbor the *KRAS* G12S mutation, the specific target of our gene editing strategy. Following intrapulmonary injection, luminescence imaging revealed the formation of small tumor nodules throughout the pulmonary tissue, confirming successful dissemination and establishment of the orthotopic disease (Fig. 5A). Once at least six animals exhibited detectable lung nodules, the efficacy study was initiated. PBS, LNP NC (0.3 mg/kg), and A6 3:1 (0.3 mg/kg) and A8 1:1 (0.3 mg/kg) Cas9 mRNA/sgRNA-LNPs were administered intratracheally twice weekly for three weeks, enabling localized delivery to the lungs and targeted assessment within the primary tumor site. At the study endpoint, lungs and blood were collected for further analyses (Fig. 5B).

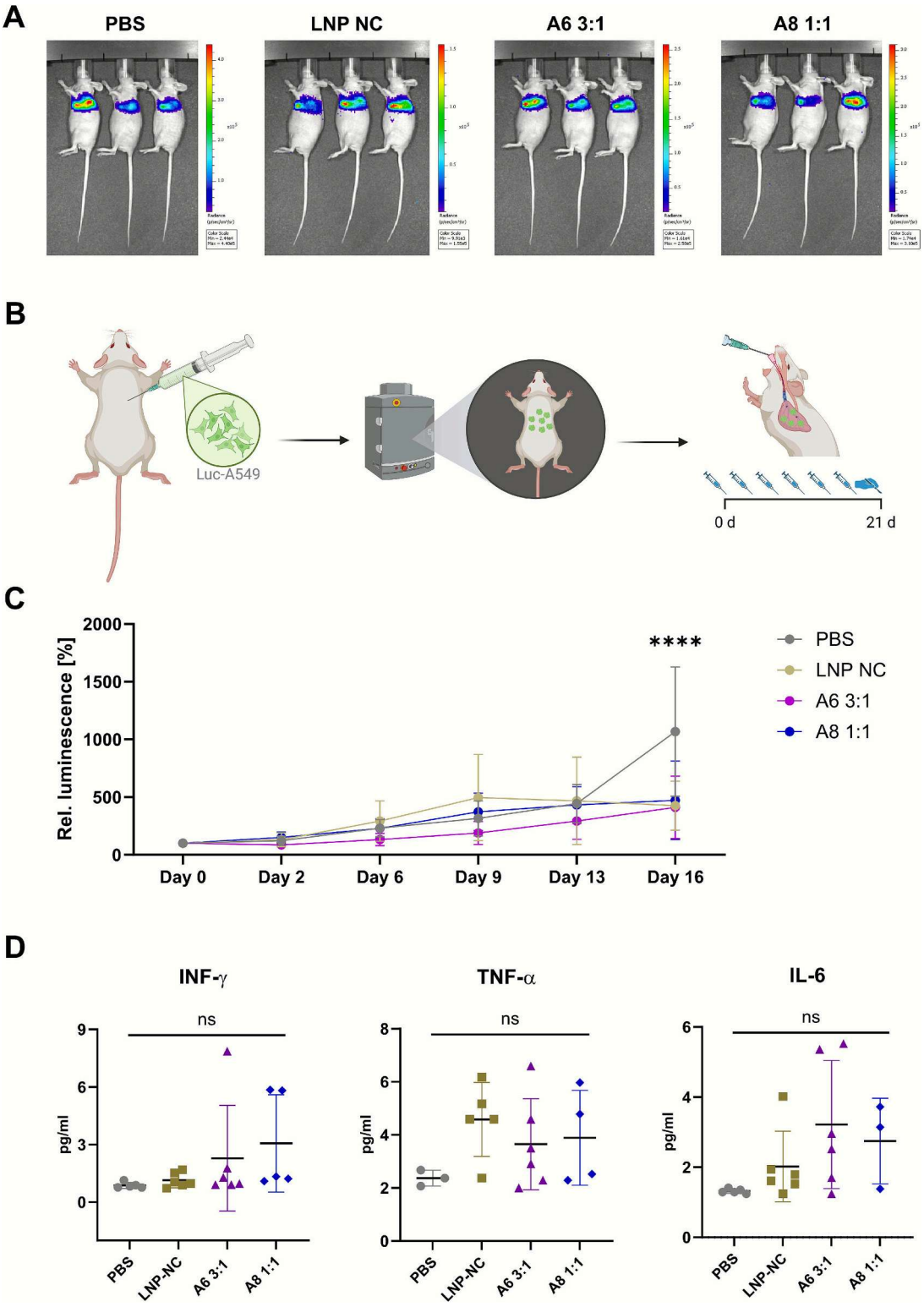

Fig. 5. Establishment of an orthotopic lung cancer model and treatment scheme for evaluating the therapeutic efficacy of Cas9 mRNA/sgRNA-loaded LNPs. **A)** Bioluminescence imaging of immunodeficient mice following intrapulmonary injection of A549-Luc cells, showing disseminated tumor nodules throughout the lungs and confirming successful model establishment. **B)** Treatment protocol: once lung nodules were detected in ≥6 animals, mice were assigned to four groups and administered intratracheally twice weekly for three weeks with PBS, LNP negative control (NC, 0.3 mg/kg), or Cas9 mRNA/sgRNA-loaded LNP formulations A6 3:1 (0.3 mg/kg) and A8 1:1 (0.3 mg/kg). At the study endpoint, lungs and blood were collected for subsequent analyses. **C)** Longitudinal monitoring of tumor progression by bioluminescence imaging, quantified as percentage increase relative to baseline signal. **D)** Systemic cytokine profiles in A549 lung tumor–bearing NMRI mice following administration of PBS, LNP NC, A6 3:1, or A8 1:1. Data are presented as mean ± SD. Statistical significance was determined using one-way ANOVA with Tukey's post-hoc test. ns: not significant.

3.5.2. Tumor progression

To assess the impact of CRISPR/Cas9-loaded LNPs on tumor progression, tumor growth was monitored *via* bioluminescence imaging and expressed as a percentage increase relative to baseline (Fig. 5C). Although no statistically significant differences in tumor growth were observed at most time points compared to the PBS group, all LNP-treated groups (NC, A6 3:1, and A8 1:1) exhibited a consistent trend toward reduced tumor burden. Notably, at day 16, tumor growth was lower in these groups relative to PBS, indicating a delayed and modest benefit in arresting tumor growth. A potential explanation for the reduction observed in the LNP-NC group is that the negative control sgRNA, despite being designed as non-targeting, may exhibit partial complementarity to murine or human transcripts. This could result in low-level off-target activity or induce cellular stress responses within tumor cells. Such unspecific recognition has been previously reported in CRISPR/Cas9 systems, where even scrambled or non-targeting guides can elicit detectable cellular effects under certain experimental conditions [60].

The modest and delayed effect size, together with partial activity in the LNP-NC group, highlights the need to interpret these findings cautiously. Two key limitations likely contribute: (1) the small sample size ($n = 6$ per group), which reduces statistical power, and (2) the limited fraction of tumor cells successfully targeted by the CRISPR/Cas9 system. These constraints demonstrate that volumetric tumor measurements alone may not fully capture early molecular or cellular responses. Therefore, to better define therapeutic activity, we extended our evaluation to downstream apoptotic signaling to provide mechanistic insight into the activity of the CRISPR/Cas9 cargo. These complementary analyses establish proof-of-concept for targeted gene editing activity *in vivo*, while also acknowledging that extended treatment regimens, larger cohorts, and longitudinal follow-up will be required to fully capture the impact on tumor burden.

3.5.3. Cytokine profile

To evaluate the systemic immunogenicity of our LNPs, we quantified serum cytokine levels in A549-cell-based lung tumor-bearing NMRI-nu mice following administration of PBS, LNP NC, and formulations A6 3:1 and A8 1:1. NMRI-nu mice harbor a Foxn1 mutation that causes thymic aplasia. This condition is characterized by a sub-development or absence of the thymus gland, which consequently results in a lack of mature αβ T cells, including Th1, Th2, Th17, and Treg subsets. This immunological background minimizes confounding T cell-driven effects, thereby allowing tumor growth following xenotransplantation and a more direct assessment of innate immune activation. Notably, B cells remain functional, and innate immune effectors such as NK cells, macrophages, dendritic cells, neutrophils, mast cells, and innate lymphoid cells are intact and active [61]. Thus, cytokine profiling in this model provides a clear readout of the innate and humoral components of LNP-induced immune responses, independent of T cell contributions. Additionally, innate immune sensors like TLRs and RIG-I-like receptors are well-characterized in murine models and are known to trigger cytokines such as IL-6, TNF-α, IFN-γ, IL-10, IL-1β, and various chemokines upon activation by nucleic acid-based stimuli, making this model highly relevant for evaluating LNP immunogenicity.

Our results showed no statistically significant differences across treatment groups for key inflammatory cytokines, including IFN-γ, TNF-α, and IL-6 (Fig. 5D). Furthermore, IL-10 levels remained below the detection threshold in all samples, indicating an absence of compensatory anti-inflammatory signaling, which often accompanies immune perturbation. These findings are consistent with our prior safety studies in healthy mice, which demonstrated no systemic toxicity based on hepatic, pancreatic, and renal biomarkers, further supporting the non-inflammatory profile of these formulations. These data indicate that LNPs A6 3:1 and A8 1:1 do not trigger overt innate immune activation *in vivo*, supporting their safety profile and suitability for continued therapeutic development.

3.5.4. Efficacy assessment

Histopathological evaluation of murine lung tissue post-treatment with Cas9 mRNA/sgRNA-LNP formulations revealed key insights into tumor pathology and therapeutic response. The H&E staining (Fig. 6A) demonstrated the presence of a well-demarcated, solid tumor mass compressing adjacent lung parenchyma, consistent with a poorly differentiated NSCLC subtype. Notably, the absence of necrosis, hemorrhage, and inflammatory infiltration across all groups demonstrates a non-immunogenic tumor phenotype, often associated with resistance to conventional therapies [62].

Next, we performed Azan staining on lung sections from A549-Luc xenograft mice. This trichrome method distinguishes cellular and stromal components, with nuclei and cytoplasm appearing red/pink and collagen-rich extracellular matrix staining blue. In the LNP NC group, lung tissue exhibited intense pink staining, indicative of high cellular density, which is consistent with active tumor proliferation or immune cell infiltration. In contrast, sections from mice treated with our LNP formulations showed a pronounced shift toward blue staining, indicative of reduced cellularity and increased deposition of fibrotic tissue (Fig. 6B). The presence of tumor-associated desmoplastic stroma is also evident, characterized by dense connective tissue surrounding or interspersed within the tumor mass. This reactive fibrosis is characteristic of tumor-stroma interactions observed in NSCLC, particularly adenocarcinomas, where stromal remodeling plays a critical role in disease progression and therapeutic response [63]. The observed increase in blue-stained fibrotic regions supports the notion that *KRAS* gene disruption not only reduces tumor cell viability but also alters the tumor microenvironment, potentially through apoptosis-induced remodeling or immune-mediated clearance. These findings are consistent with prior reports demonstrating that stromal reorganization and desmoplasia are hallmarks of NSCLC and can be modulated by effective therapeutic intervention [64].

To further characterize the tumor microenvironment in our A549-Luc xenograft model, we performed PAS staining, which highlights neutral mucins and glycoproteins within tissue sections. Tumor cells in all groups exhibited strong PAS-positive cytoplasmic staining (Fig. 6C), consistent with intracellular accumulation of neutral mucins, which is a hallmark of mucinous adenocarcinomas and *KRAS*-driven lung tumors. Notably, no luminal PAS-positive secretion was observed, reinforcing the interpretation that mucins were retained intracellularly rather than secreted into glandular spaces. Histological comparison revealed a more pronounced pinkish PAS signal in the PBS-treated control group, while LNP-treated groups appeared to exhibit reduced staining intensity (Fig. 6C). Although these differences were not quantified and should be interpreted cautiously, the observed trend may reflect alterations in mucin dynamics, potentially due to reduced mucin synthesis or increased degradation following *KRAS* gene disruption. *KRAS* mutations are known to regulate mucin gene expression, particularly MUC5AC and MUC1, which contribute to tumor progression and immune evasion [65]. Therefore, the apparent reduction in PAS signal in treated groups may suggest a shift in tumor cell phenotype and a possible attenuation of oncogenic signaling.

As discussed above, apoptosis is a key downstream consequence of *KRAS* disruption, especially in oncogene-addicted tumors such as *KRAS*-mutant NSCLC (Fig. 6E). As illustrated in the figure, wild-type KRAS (Figure 6Ei) cycles between inactive and active states in response to upstream signals, thereby regulating key cellular processes such as cell survival and proliferation. In contrast, *KRAS* G12S mutations lock the protein in a constitutively active state, driving persistent proliferative signaling (Figure 6Eii). Gene editing disrupts this oncogenic activity, resulting in a loss-of-function phenotype (Figure 6Eiii) that removes critical survival cues and shifts the cellular balance toward apoptosis.

To evaluate whether our gene editing strategy translated into functional cell death *in vivo*, we performed TUNEL staining on lung sections from A549-Luc xenograft mice. The TUNEL assay detects DNA fragmentation, characteristic of late-stage apoptosis, by labeling free 3′-

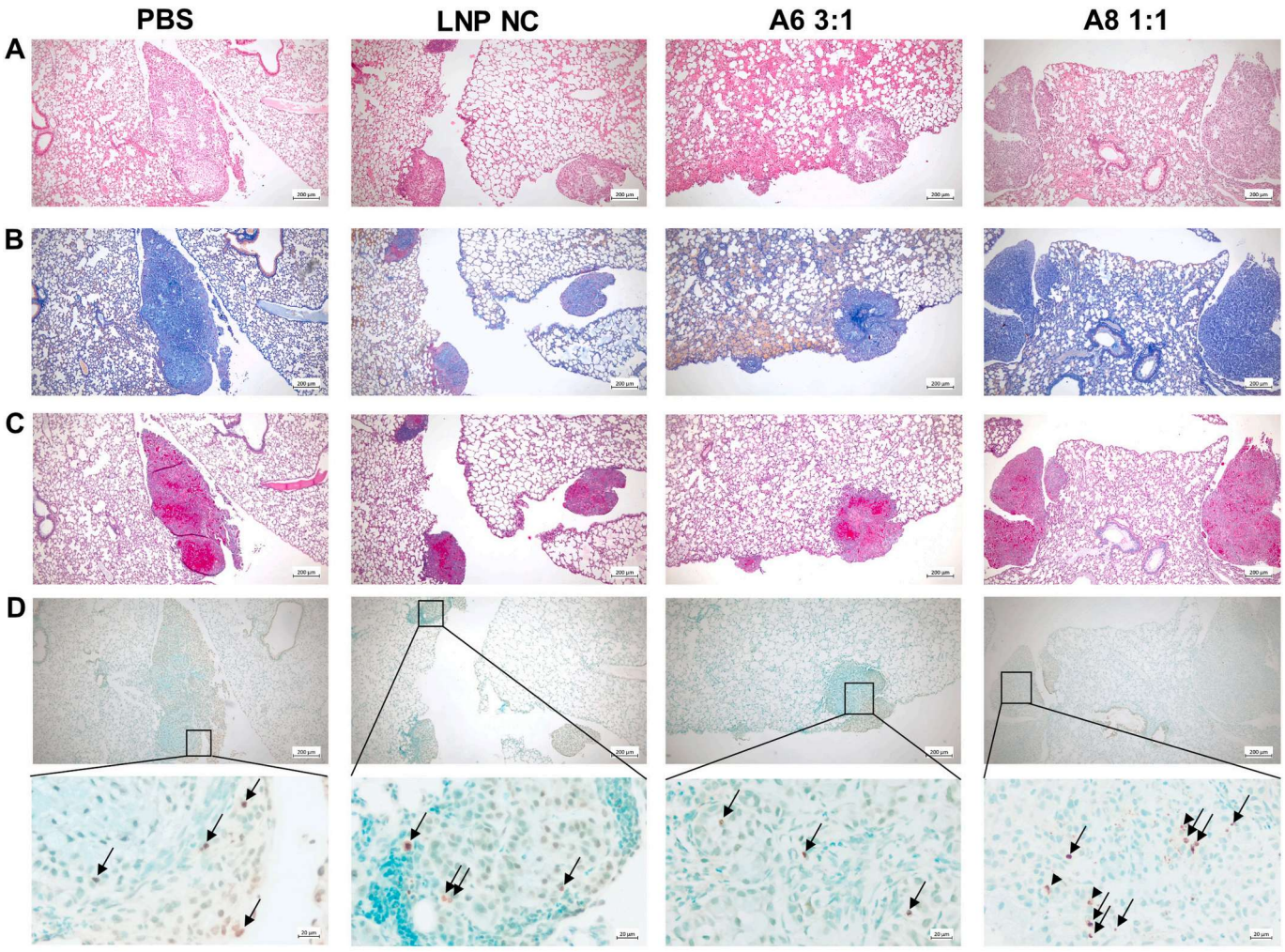

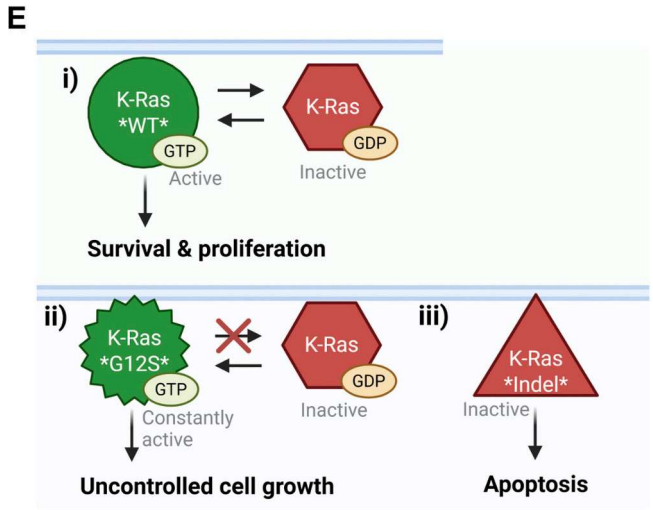

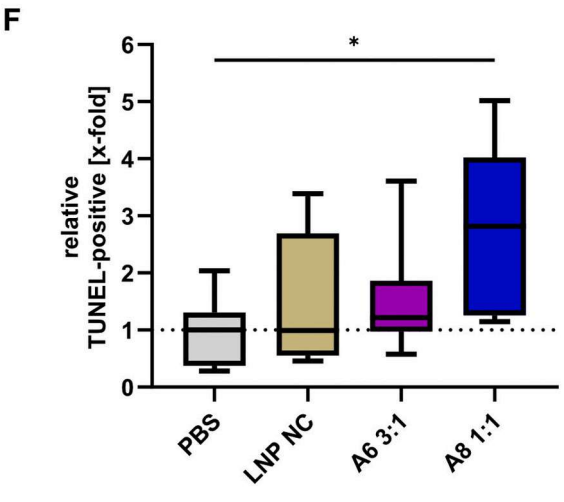

Fig. 6. Histological evaluation of lung tumors following treatment with Cas9 mRNA/sgRNA-LNPs. Tumor sections from mice treated with PBS, LNP-NC, A6 3:1, or A8 1:1 were stained with **A)** Hematoxylin and Eosin (H&E) to assess general morphology, **B)** Azan to visualize desmoplastic stroma, **C)** Periodic Acid–Schiff (PAS) to detect mucopolysaccharides and glycogen, and **D)** TUNEL assay to evaluate apoptosis. Representative images are shown for each group. **E)** Mechanistic basis of apoptosis induction following *KRAS* G12S disruption. Schematic representation showing i) balanced signaling of wild-type KRAS, ii) constitutive activation of mutant KRAS G12S driving uncontrolled proliferation, and iii) gene editing-mediated disruption of oncogenic *KRAS* signaling, resulting in loss of survival cues and induction of apoptosis. **F)** Quantification of TUNEL assay. Relative TUNEL-positive nuclei are expressed as fold-change values normalized to PBS controls across all treatment groups. Data are presented as mean ± SD. Statistical significance was determined using one-way ANOVA with Tukey's post-hoc test (*$p < 0.05$).

hydroxyl termini in cleaved chromatin [66]. Histological analysis revealed TUNEL-positive nuclei (brown) within the tumor mass across all groups, indicating the presence of apoptotic cells (Fig. 6D). Notably, the LNP A8 1:1-treated group exhibited a higher density of apoptotic bodies (arrowheads), suggesting more extensive apoptotic activity. While apoptosis appeared focal rather than diffuse, the presence of these apoptotic structures is consistent with localized tumor cell death and remodeling of the tumor microenvironment. These observations were corroborated by quantification analysis, which confirmed statistically significant increases in apoptotic bodies compared to other groups (Fig. 6F). Specifically, A8 1:1 exhibited a ~ 3.0-fold increase in TUNEL-positive nuclei relative to PBS, demonstrating its efficacy in disrupting KRAS signaling and driving robust pro-apoptotic activity. These findings are particularly promising given the central role of KRAS in regulating cell survival pathways. *KRAS* mutations suppress apoptosis by upregulating anti-apoptotic proteins such as Bcl-xL and survivin [67]. Therefore, the induction of apoptosis following *KRAS* gene editing provides evidence of therapeutic efficacy and pathway-specific disruption. The evident presence of apoptotic bodies in the A8 1:1 group further supports the pro-apoptotic activity of this formulation and its potential as a targeted therapeutic strategy for *KRAS*-mutant malignancies.

3.6. Scaling challenges

The study provides a novel proof-of-concept for the treatment of *KRAS G12S* mutations in NSCLC. Although the formulation represents a promising therapeutic approach, key translational challenges remain to be addressed. The first relates to aerosol performance, which is fundamental for pulmonary administration. Among available technologies, nebulization for liquid aerosols and spray-drying for dry powder formulations are currently considered the most suitable strategies. However, both approaches require further optimization of operational parameters and excipient selection to ensure consistent performance and long-term stability [68–70]. A second challenge concerns interaction with human airway mucus. While formulations A6 and A8 were able to transport through the mucin-rich environment and achieved cellular uptake, the pronounced inter-individual and regional heterogeneity of human airway mucus could markedly influence delivery efficiency [58]. Addressing these challenges will be essential to advance the formulations from proof-of-concept toward clinical translation.

4. Conclusion

This study provides a structural approach for the design and evaluation of LNPs tailored for pulmonary delivery of gene editing therapeutics in targeting *KRAS* G12S in NSCLC. By optimizing lipid molar ratios, we developed and screened a library of LNPs using eGFP mRNA as a surrogate for CRISPR/Cas9 cargo, identifying formulations A6 and A8 as lead candidates. Subsequent optimization of Cas9 mRNA/sgRNA ratios further enhanced their performance. These formulations exhibited distinct morphological features, high gene editing efficiency, and robust downstream responses *in vitro*, along with enhanced transport across airway mucus barriers, properties that likely contribute to their superior transfection efficiency. *In vivo*, both candidates demonstrated good tolerability, with no significant alterations in systemic toxicity markers. Tumor progression was moderately attenuated, and histological analysis of lung nodules revealed increased apoptosis consistent with on-target CRISPR/Cas9 activity. Notably, formulation A8 1:1 achieved the most robust and reproducible activity across *in vitro* and *in vivo* models, validating its promise as a clinically relevant vehicle for localized gene editing in the lung.

Looking forward, mechanistic studies of A8 1:1-mediated apoptosis and evaluation of long-term survival benefit in tumor-bearing models will be critical. In parallel, advancing delivery strategies, particularly *via* vibrating-mesh nebulization and spray drying, will be essential to address key translational hurdles. These efforts will help determine whether the observed molecular activity can be advanced toward patient-centered, non-invasive administration of RNA-based precision therapies for NSCLC.

CRediT authorship contribution statement

Moritz Marschhofer: Writing – review & editing, Writing – original draft, Visualization, Validation, Methodology, Investigation, Formal analysis. **Siyu Chen:** Methodology, Investigation, Formal analysis. **Müge Molbay:** Writing – review & editing, Investigation, Formal analysis. **Benjamin Winkeljann:** Writing – review & editing. **Ersilia Villano:** Investigation. **Corinne Giancaspro:** Investigation, Formal analysis. **Alexandra Kourou:** Investigation, Formal analysis. **Otto Berninghausen:** Investigation. **Susanne Rieder:** Investigation. **Charlotte Ungewickell:** Investigation. **Roland Beckmann:** Resources. **Bastian Popper:** Writing – review & editing, Investigation. **Ana Maria Torres:** Methodology, Investigation. **Anxo Vidal:** Methodology, Investigation. **Olivia M. Merkel:** Writing – review & editing, Supervision, Resources. **Simone P. Carneiro:** Writing – review & editing, Writing – original draft, Supervision, Funding acquisition, Formal analysis, Conceptualization.

Declaration of generative AI and AI-assisted technologies in the writing process

During the preparation of this work, the authors used AI in order to enhance the readability and language. After using this tool, the authors reviewed and edited the content as needed and take full responsibility for the content of the published article.

Funding

This work was supported by funding from the Alexander von Humboldt Foundation, LMU (LMUexcellent), and the European Research Council (ERC-2022-COG-101088587).

Declaration of competing interest

Olivia Merkel and Benjamin Winkeljann are co-founders of RNhale GmbH. Olivia Merkel is a scientific advisory board member of Coriolis Pharma, AMW, and Corden Pharma, as well as a consultant for PARI Pharma, AbbVie Deutschland, and Boehringer-Ingelheim International.

The authors declare no competing financial interest.

Acknowledgements

Simone Carneiro gratefully thanks the financial support from the Alexander von Humboldt Foundation and the LMUexcellent strategy. We would like to thank Prof. Vollmar for kindly gifting the A549 cell line. Certain graph elements were created with Biorender. Lab, M. (2025).

Appendix A. Supplementary data

Supplementary data to this article can be found online at https://doi.org/10.1016/j.jconrel.2026.114607.

Data availability

Data will be made available upon request.

References

[1] H. Sung, J. Ferlay, R.L. Siegel, et al., Global Cancer statistics 2020: GLOBOCAN estimates of incidence and mortality worldwide for 36 cancers in 185 countries, CA Cancer J. Clin. 71 (2021) 209–249, https://doi.org/10.3322/caac.21660.

[2] W. Pao, N. Girard, New driver mutations in non-small-cell lung cancer, Lancet Oncol. 12 (2011) 175–180, https://doi.org/10.1016/S1470-2045(10)70087-5.
[3] J. Judd, N. Abdel Karim, H. Khan, et al., Characterization of KRAS mutation subtypes in non–small cell lung Cancer, Mol. Cancer Ther. 20 (2021) 2577–2584, https://doi.org/10.1158/1535-7163.MCT-21-0201.
[4] S.C. Lau, N. Chooback, C. Ho, et al., Outcome differences between first- and second-generation EGFR inhibitors in advanced *EGFR* mutated NSCLC in a large population-based cohort, Clin. Lung Cancer 20 (2019) e576–e583, https://doi.org/10.1016/j.cllc.2019.05.003.
[5] M. Khan, J. Lin, G. Liao, et al., ALK inhibitors in the treatment of ALK positive NSCLC, Front. Oncol. (2019) 8, https://doi.org/10.3389/fonc.2018.00557.
[6] FDA, Highlights of Prescribing Information KRAZATI® (adagrasib). https://www.accessdata.fda.gov/drugsatfda_docs/label/2024/216340s005lbl.pdf, 2025 (accessed April 13, 2025).
[7] FDA, Highlights of Prescribing Information LUMAKRAS® (sotorasib). https://www.accessdata.fda.gov/drugsatfda_docs/label/2025/214665Orig1s009correctedlbl.pdf, 2025.
[8] M.M. Awad, S. Liu, I.I. Rybkin, et al., Acquired resistance to KRASG12C inhibition in Cancer, N. Engl. J. Med. (2021), https://doi.org/10.1056/NEJMoa2105281.
[9] T. Koga, K. Suda, T. Fujino, et al., *KRAS* secondary mutations that confer acquired resistance to KRAS G12C inhibitors, Sotorasib and Adagrasib, and overcoming strategies: insights from in vitro experiments, J. Thorac. Oncol. 16 (2021) 1321–1332, https://doi.org/10.1016/j.jtho.2021.04.015.
[10] A. Di Federico, I. Ricciotti, V. Favorito, et al., Resistance to KRAS G12C inhibition in non-small cell lung Cancer, Curr. Oncol. Rep. 25 (2023) 1017–1029, https://doi.org/10.1007/s11912-023-01436-y.
[11] M. Jinek, K. Chylinski, I. Fonfara, et al., A programmable dual-RNA–guided DNA endonuclease in adaptive bacterial immunity, Science 337 (2012) 816–821, https://doi.org/10.1126/science.1225829.
[12] E. Deltcheva, K. Chylinski, C.M. Sharma, et al., CRISPR RNA maturation by trans-encoded small RNA and host factor RNase III, Nature 471 (2011) 602–607, https://doi.org/10.1038/nature09886.
[13] K. Rodgers, M. McVey, Error-prone repair of DNA double-Strand breaks, J. Cell. Physiol. 231 (2016) 15–24, https://doi.org/10.1002/jcp.25053.
[14] D.G. MacArthur, C. Tyler-Smith, Loss-of-function variants in the genomes of healthy humans, Hum. Mol. Genet. 19 (2010) R125–R130, https://doi.org/10.1093/hmg/ddq365.
[15] S.P. Carneiro, A. Greco, E. Chiesa, et al., Shaping the future from the small scale: dry powder inhalation of CRISPR-Cas9 lipid nanoparticles for the treatment of lung diseases, Expert Opin. Drug Deliv. 20 (2023) 471–487, https://doi.org/10.1080/17425247.2023.2185220.
[16] X. Liu, Z. Zhao, F. Wu, et al., Tailoring Hyperbranched poly(β-amino ester) as a robust and universal platform for cytosolic protein delivery, Adv. Mater. 34 (2022) 2108116, https://doi.org/10.1002/adma.202108116.
[17] A. Mehta, O.M. Merkel, Immunogenicity of Cas9 protein, J. Pharm. Sci. 109 (2020) 62–67, https://doi.org/10.1016/j.xphs.2019.10.003.
[18] FDA, Highlights of Prescribing Information (Comirnaty). https://www.fda.gov/media/151707/download?attachment, 2024 (accessed February 11, 2025).
[19] FDA, Fact Sheet for Healthcare Providers Administering Vaccine: Emergency Use Authorization of Moderna COVID-19 Vaccine (2024–2025 Formula), for Individuals 6 Months Through 11 Years of Age, 2024.
[20] A.-G. Reinhart, A. Osterwald, P. Ringler, et al., Investigations into mRNA lipid nanoparticles shelf-life stability under nonfrozen conditions, Mol. Pharm. 20 (2023) 6492–6503, https://doi.org/10.1021/acs.molpharmaceut.3c00956.
[21] L. Xue, A.G. Hamilton, G. Zhao, et al., High-throughput barcoding of nanoparticles identifies cationic, degradable lipid-like materials for mRNA delivery to the lungs in female preclinical models, Nat. Commun. 15 (2024) 1884, https://doi.org/10.1038/s41467-024-45422-9.
[22] FDA, Highlights of Prescribing Information (Casgevy). https://pi.vrtx.com/files/uspi_exagamglogene_autotemcel.pdf, 2024 (accessed August 5, 2025).
[23] J.D. Gillmore, E. Gane, J. Taubel, et al., CRISPR-Cas9 in vivo gene editing for transthyretin amyloidosis, N. Engl. J. Med. 385 (2021) 493–502, https://doi.org/10.1056/NEJMoa2107454.
[24] D.M. Cohn, P. Gurugama, M. Magerl, et al., CRISPR-based therapy for hereditary angioedema, N. Engl. J. Med. 392 (2025) 458–467, https://doi.org/10.1056/NEJMoa2405734.
[25] Verve Therapeutics, Inc, Open-label, Phase 1b, Single Ascending Dose Study to Evaluate the Safety of VERVE-102 Administered to Patients with Heterozygous Familial Hypercholesterolemia or Premature Coronary Artery Disease Who Require Additional Lowering of Low-density Lipoprotein Cholesterol, clinicaltrials.gov, 2024.
[26] L. Schoenmaker, D. Witzigmann, J.A. Kulkarni, et al., mRNA-lipid nanoparticle COVID-19 vaccines: structure and stability, Int. J. Pharm. 601 (2021) 120586, https://doi.org/10.1016/j.ijpharm.2021.120586.
[27] FDA, Highlights of Prescribing Information (Onpattro). https://www.accessdata.fda.gov/drugsatfda_docs/label/2018/210922s000lbl.pdf#page=8.22, 2018 (accessed February 11, 2025).
[28] S. Omo-Lamai, M.E. Zamora, M.N. Patel, et al., Physicochemical targeting of lipid nanoparticles to the lungs induces clotting: mechanisms and solutions, Adv. Mater. 36 (2024) 2312026, https://doi.org/10.1002/adma.202312026.
[29] J. Kim, A. Jozic, Y. Lin, et al., Engineering lipid nanoparticles for enhanced intracellular delivery of mRNA through inhalation, ACS Nano 16 (2022) 14792–14806, https://doi.org/10.1021/acsnano.2c05647.
[30] L. Yue, X. Zhang, C. Zhao, et al., Inhaled drug delivery: past, present, and future, Nano Today 52 (2023) 101942, https://doi.org/10.1016/j.nantod.2023.101942.
[31] S.P. Carneiro, J.T. Müller, O.M. Merkel, Fluorescent techniques for RNA detection in nanoparticles, in: M. Astatke (Ed.), RNA Amplif. Anal. Methods Protoc, Springer US, New York, NY, 2024, pp. 187–203, https://doi.org/10.1007/978-1-0716-3918-4_14.
[32] S. Rademacker, S. Pinto Carneiro, M. Molbay, et al., The impact of lipid compositions on siRNA and mRNA lipid nanoparticle performance for pulmonary delivery, Eur. J. Pharm. Sci. 212 (2025) 107182, https://doi.org/10.1016/j.ejps.2025.107182.
[33] D. Conant, T. Hsiau, N. Rossi, et al., Inference of CRISPR edits from sanger trace data, CRISPR J. 5 (2022) 123–130, https://doi.org/10.1089/crispr.2021.0113.
[34] E. Borrajo, R. Abellan-Pose, A. Soto, et al., Docetaxel-loaded polyglutamic acid-PEG nanocapsules for the treatment of metastatic cancer, J. Control. Release 238 (2016) 263–271, https://doi.org/10.1016/j.jconrel.2016.07.048.
[35] S. Chen, M. Triki, S. Pinto Carneiro, et al., A novel micelleplex for tumour-targeted delivery of CRISPR-Cas9 against KRAS-mutated lung cancer, Nanoscale 17 (2025) 6604–6619, https://doi.org/10.1039/D4NR03471F.
[36] K.J. Kauffman, J.R. Dorkin, J.H. Yang, et al., Optimization of lipid nanoparticle formulations for mRNA delivery in vivo with fractional factorial and definitive screening designs, Nano Lett. 15 (2015) 7300–7306, https://doi.org/10.1021/acs.nanolett.5b02497.
[37] H. Liu, M.Z. Chen, T. Payne, et al., Beyond the endosomal bottleneck: understanding the efficiency of mRNA/LNP delivery, Adv. Funct. Mater. 34 (2024) 2404510, https://doi.org/10.1002/adfm.202404510.
[38] S.C. Semple, A. Akinc, J. Chen, et al., Rational design of cationic lipids for siRNA delivery, Nat. Biotechnol. 28 (2010) 172–176, https://doi.org/10.1038/nbt.1602.
[39] A.E. Zelkoski, Z. Lu, G. Sukumar, et al., Ionizable lipid nanoparticles of mRNA vaccines elicit NF-κB and IRF responses through toll-like receptor 4, Npj Vaccines 10 (2025) 73, https://doi.org/10.1038/s41541-025-01124-x.
[40] D. Wang, F. Zhang, G. Gao, CRISPR-based therapeutic genome editing: strategies and in vivo delivery by AAV vectors, Cell 181 (2020) 136–150, https://doi.org/10.1016/j.cell.2020.03.023.
[41] Y. Li, R. Tian, J. Xu, et al., Recent developments of polymeric delivery systems in gene therapeutics, Polym. Chem. 15 (2024) 1908–1931, https://doi.org/10.1039/D4PY00124A.
[42] A.K.K. Leung, I.M. Hafez, S. Baoukina, et al., Lipid nanoparticles containing siRNA synthesized by microfluidic mixing exhibit an Electron-dense nanostructured Core, J. Phys. Chem. C 116 (2012) 18440–18450, https://doi.org/10.1021/jp303267y.
[43] M.H.Y. Cheng, J. Leung, Y. Zhang, et al., Induction of bleb structures in lipid nanoparticle formulations of mRNA leads to improved transfection potency, Adv. Mater. 35 (2023) 2303370, https://doi.org/10.1002/adma.202303370.
[44] M.H.Y. Cheng, Y. Zhang, K. Fox, et al., Liposomal lipid nanoparticles for extrahepatic delivery of mRNA, Nat. Commun. 16 (2025) 4135, https://doi.org/10.1038/s41467-025-58523-w.
[45] D.S. Karaman, D. Desai, R. Senthilkumar, et al., Shape engineering vs organic modification of inorganic nanoparticles as a tool for enhancing cellular internalization, Nanoscale Res. Lett. 7 (2012) 358, https://doi.org/10.1186/1556-276X-7-358.
[46] C.A. Little, C. Batchelor-McAuley, N.P. Young, et al., Shape and size of non-spherical silver nanoparticles: implications for calculating nanoparticle number concentrations, Nanoscale 10 (2018) 15943–15947, https://doi.org/10.1039/C8NR06062B.
[47] P.A. Hassan, S. Rana, G. Verma, Making sense of Brownian motion: colloid characterization by dynamic light scattering, Langmuir 31 (2015) 3–12, https://doi.org/10.1021/la501789z.
[48] Q. Gao, W. Ouyang, B. Kang, et al., Selective targeting of the oncogenic KRAS G12S mutant allele by CRISPR/Cas9 induces efficient tumor regression, Theranostics 10 (2020) 5137–5153, https://doi.org/10.7150/thno.42325.
[49] D.G. Miller, L.M. Petek, D.W. Russell, Adeno-associated virus vectors integrate at chromosome breakage sites, Nat. Genet. 36 (2004) 767–773, https://doi.org/10.1038/ng1380.
[50] E. Atsavapranee, R.M. Haley, M.M. Billingsley, et al., Ionizable lipid nanoparticles for RAS protease delivery to inhibit cancer cell proliferation, J. Control. Release 370 (2024) 614–625, https://doi.org/10.1016/j.jconrel.2024.05.015.
[51] K. Syama, Z.J. Jakubek, S. Chen, et al., Development of lipid nanoparticles and liposomes reference materials (II): cytotoxic profiles, Sci. Rep. 12 (2022) 18071, https://doi.org/10.1038/s41598-022-23013-2.
[52] S. Omo-Lamai, Y. Wang, M.N. Patel, et al., Limiting endosomal damage sensing reduces inflammation triggered by lipid nanoparticle endosomal escape, Nat. Nanotechnol. (2025) 1–13, https://doi.org/10.1038/s41565-025-01974-5.
[53] J. Ahn, C.-S. Cho, S.W. Cho, et al., Investigation on vascular cytotoxicity and extravascular transport of cationic polymer nanoparticles using perfusable 3D microvessel model, Acta Biomater. 76 (2018) 154–163, https://doi.org/10.1016/j.actbio.2018.05.041.
[54] H.J. Kim, H.N. Lee, M.S. Jeong, et al., Oncogenic KRAS: signaling and drug resistance, Cancers 13 (2021) 5599, https://doi.org/10.3390/cancers13225599.
[55] X. Guo, H. Wang, Y. Li, et al., Transfection reagent Lipofectamine triggers type I interferon signaling activation in macrophages, Immunol. Cell Biol. 97 (2019) 92–96, https://doi.org/10.1111/imcb.12194.
[56] D. Bertheloot, E. Latz, B.S. Franklin, Necroptosis, pyroptosis and apoptosis: an intricate game of cell death, Cell. Mol. Immunol. 18 (2021) 1106–1121, https://doi.org/10.1038/s41423-020-00630-3.
[57] J.-H. Bang, S. Lee, N.-J. Kim, et al., Effect of aerosolized benzalkonium chloride exposure in in vitro cell models using air–liquid interface culture for inhalation toxicity screening, Toxicol. Res. (2025), https://doi.org/10.1007/s43188-025-00315-x.

[58] E. Meziu, M. Koch, J. Fleddermann, et al., Visualization of the structure of native human pulmonary mucus, Int. J. Pharm. 597 (2021) 120238, https://doi.org/10.1016/j.ijpharm.2021.120238.
[59] T. Wei, Y. Sun, Q. Cheng, et al., Lung SORT LNPs enable precise homology-directed repair mediated CRISPR/Cas genome correction in cystic fibrosis models, Nat. Commun. 14 (2023) 7322, https://doi.org/10.1038/s41467-023-42948-2.
[60] J.G. Doench, N. Fusi, M. Sullender, et al., Optimized sgRNA design to maximize activity and minimize off-target effects of CRISPR-Cas9, Nat. Biotechnol. 34 (2016) 184–191, https://doi.org/10.1038/nbt.3437.
[61] Janvier Labs, NMRI-Nu Mouse. https://janvier-labs.com/wp-content/uploads/NMRI-nu-mouse_06_08_21_Janvier_Labs_EN.pdf, 2025. (Accessed 19 August 2025).
[62] G. Song, C. Shang, L. Sun, et al., Ad-VT enhances the sensitivity of chemotherapy-resistant lung adenocarcinoma cells to gemcitabine and paclitaxel in vitro and in vivo, Investig. New Drugs 40 (2022) 274–289, https://doi.org/10.1007/s10637-021-01204-4.
[63] R.M. Bremnes, T. Dønnem, S. Al-Saad, et al., The role of tumor stroma in Cancer progression and prognosis: emphasis on carcinoma-associated fibroblasts and non-small cell lung cancer, J. Thorac. Oncol. 6 (2011) 209–217, https://doi.org/10.1097/JTO.0b013e3181f8a1bd.
[64] S. Zuo, M. Wei, S. Wang, et al., Pan-cancer analysis of immune cell infiltration identifies a prognostic immune-cell characteristic score (ICCS) in lung adenocarcinoma, Front. Immunol. (2020) 11, https://doi.org/10.3389/fimmu.2020.01218.
[65] T.M. Horm, J.A. Schroeder, MUC1 and metastatic cancer: expression, function and therapeutic targeting, Cell Adhes. Migr. 7 (2013) 187–198, https://doi.org/10.4161/cam.23131.
[66] K. Kyrylkova, S. Kyryachenko, M. Leid, et al., Detection of apoptosis by TUNEL assay, in: C. Kioussi (Ed.), Odontogenesis Methods Protoc, Humana Press, Totowa, NJ, 2012, pp. 41–47, https://doi.org/10.1007/978-1-61779-860-3_5.
[67] A. Ferreira, F. Pereira, C. Reis, et al., Crucial role of oncogenic KRAS mutations in apoptosis and autophagy regulation: therapeutic implications, Cells 11 (2022) 2183, https://doi.org/10.3390/cells11142183.
[68] C.M. Zimmermann, D. Baldassi, K. Chan, et al., Spray drying siRNA-lipid nanoparticles for dry powder pulmonary delivery, J. Control. Release 351 (2022) 137–150, https://doi.org/10.1016/j.jconrel.2022.09.021.
[69] J.B. Heiser, M. Lewis, M.M. Zerankeshi, et al., Systematic screening of excipients to stabilize aerosolized lipid nanoparticles for enhanced mRNA delivery, RSC Pharm. (2025), https://doi.org/10.1039/D5PM00061K.
[70] A. Sarode, P. Patel, N. Vargas-Montoya, et al., Inhalable dry powder product (DPP) of mRNA lipid nanoparticles (LNPs) for pulmonary delivery, Drug Deliv. Transl. Res. 14 (2024) 360–372, https://doi.org/10.1007/s13346-023-01402-y.